

University of Nevada, Reno

Analysis of fault rupture potential resulting from large-scale groundwater withdrawal: application to Spring Valley, Nevada

A thesis submitted in partial fulfillment of the requirements for the degree of Master of Science in Hydrogeology

By

Brian Anderson

Dr. Rina Schumer / Thesis Advisor

August 2016

© by Brian J. Anderson 2016

All Rights Reserved



THE GRADUATE SCHOOL

We recommend that the thesis
prepared under our supervision by

BRIAN J. ANDERSON

Entitled

**Analysis of fault rupture potential resulting from large-scale groundwater
withdrawal: application to Spring Valley, Nevada**

be accepted in partial fulfillment of the
requirements for the degree of

MASTER OF SCIENCE

Rina Schumer, Ph.D., Advisor

Scott McCoy, Ph.D., Committee Member

William Hammond, Ph.D., Committee Member

Alexandra Lutz, Ph.D., Graduate School Representative

David W. Zeh, Ph. D., Dean, Graduate School

August, 2016

Abstract

Hydrospheric mass changes create subsurface stress perturbations on a scale that can trigger seismic events or accelerate frequency of seismicity on proximal faults. For example, groundwater pumping has been implicated in the 2011 M_w 5.1 earthquake in Lorca, Spain and the 2010 M_w 7.1 El-Mayor Cucapah earthquake in northern Baja California. Previous work on effects of pumping on seismicity is retrospective. We propose a method to assess changes in rupture potential on faults near areas of large-scale groundwater withdrawal before pumping begins. Changes in potentiometric head due to pumping predicted by (MODFLOW) groundwater flow models can be used as the change in surface load input for analytical solutions from Boussinesq [1885] to resolve changes in the subsurface state of stress. Coulomb stress, which quantifies a fault's tendency toward failure, is then resolved on proximal faults. These stress changes can be compared with a 10 kPa stress threshold developed in previous work from statistical correlation of aftershock occurrence with spatial patterns of post-seismic Coulomb stress change on surrounding faults. Stress changes on critical to near-critically stressed faults above the threshold represent a higher likelihood of seismic rupture. The method is applied to a proposed groundwater development project in Spring Valley, Nevada. Proposed pumping in excess of 50 years will result in stress change on the proximal normal fault exceeding the 10 kPa threshold. This change in Coulomb stress is in the realm of earthquake-inducing pumping. However, the low seismic hazard in the region determined from geodetic and paleoseismic analysis does not suggest imminent rupture.

Acknowledgements

Many thanks to the Nevada Water Resources Research Institute for funding the project and especially for investing in aspiring water-related professionals such as myself.

Thanks to my advisors, Rina and Scott, for their direction and always-helpful feedback, as well as guiding me along the way.

Thanks to my committee members Bill and Alex for helping me by reviewing proposal and thesis revisions and providing insight from each of your fields.

Thanks also to Keith Halford for being willing to help by altering his MODFLOW model to include points of diversion in Spring Valley. Without his easily accessible model the project would have been much more difficult to complete.

Lastly, thanks to my wife Rachel for her support and encouragement along the way, as well as my son James for giving me increased inspiration for completion of a successful project.

Table of Contents

Abstract	i
Acknowledgements	ii
List of Tables	iv
List of Figures	iv
Introduction	1
Mechanics of stress transfer/stress change	1
Background (previous studies)	3
Previous study methods	8
Shallow pumping / shallow drawdown (relative to seismogenic depths)	10
Fault Rupture Triggering Thresholds	11
Methods	14
Static stress change modeling using the assumption of a two-dimensional (2D) surface load	14
3D static stress change modeling using groundwater modeling	16
Case Study: Spring Valley	19
Spring Valley description	20
Spring Valley Faults and tectonics	23
Schell Creek Range fault	23
Southern Spring Valley fault zone	23
Tectonics	24
Groundwater flow model description	24
Scenarios modeled	29
2D model description	30
3D model description	31
Discussion	39
Comparison of 2D vs. 3D stress modeling results	39
Comparison of normal and strike slip motion	40
Comparison of Coulomb stress change in Spring Valley case study with previous study results	41
Method applications	42
Considerations under the given method	43
Conclusions	44

References	46
-------------------------	----

List of Tables

Table 1. Comparison of studies implicating groundwater pumping as cause of earthquake rupture

List of Figures

Figure 1. Mohr circle diagram of stress change from loading/unloading cycles. Before loading, the stress state in the crust is near failure [from Hampel and Hetzel, 2006]..... 4

Figure 2. Rate of surface stress change $\Delta\sigma\Delta t$ versus the change in surface stress for a variety of natural and anthropogenic crustal unloading events..... 7

Figure 3. Schematic diagram of mechanisms for inducing earthquakes. Earthquakes may be induced by increasing the pore pressure acting on a fault (**left**) or by changing the shear and normal stress acting on the fault (**right**) [from Ellsworth, 2013]..... 11

Figure 4. Geometry and sense of stress for two-dimensional subsurface stress modeling equations after Jaeger et al. [2007]..... 15

Figure 5. Spring Valley and surrounding ranges. Quaternary faults are shown in red as catalogued by the United States Geological Survey and the Nevada Bureau of Mines and Geology [USGS & NBMG, 2016]. Points of diversion corresponding to State-Engineer granted permits for municipal water use in the Las Vegas area are marked as points on the map..... 22

Figure 6. Halford & Plume [2011] (figure 10) sample model construction showing layers 1-4. Layer 1 is 3.05 m thick, layer 2 is 15.25 m thick, and layers 3 and 4 vary in thickness but do not exceed 610 m in thickness. 25

Figure 7. Drawdown (in feet) from pumping at a rate of $75.4 \times 10^6 \text{ m}^3/\text{year}$ ($\sim 61,127$ acre-feet/year) for **10** years from Halford & Plume [2011] with points of diversion modified to locations in accordance with the Office of the Nevada State Engineer applications 54003 to 54021 in Spring Valley..... 27

Figure 8. Drawdown (in feet) from pumping at a rate of $75.4 \times 10^6 \text{ m}^3/\text{year}$ ($\sim 61,127$ acre-feet/year) for **50** years from Halford & Plume [2011] with points of diversion modified to locations in accordance with the Office of the Nevada State Engineer applications 54003 to 54021 in Spring Valley..... 28

Figure 9. Drawdown (in feet) from pumping at a rate of $75.4 \times 10^6 \text{ m}^3/\text{year}$ ($\sim 61,127$ acre-feet/year) for **100** years from Halford & Plume [2011] with points of diversion modified to locations in accordance with the Office of the Nevada State Engineer applications 54003 to 54021 in Spring Valley..... 29

Figure 10. Vertical Δ CFF profile from the Schell Creek Range fault and southern Spring Valley fault zone. Δ CFF is plotted for various valley widths (2a in equations 4-6).....	31
Figure 11. Schematic of model setup and methods.....	32
Figure 12. (Left) Layout of 3D model grid over Spring Valley (right) 2D rectangular load assumptions. The red outline is for 20 km load width assumption, and pink represents a 40 km load width assumption.	33
Figure 13. Δ CFF contoured in the fault plane of the SCRf and the SSVFC for 10 year scenario. Distance increases southward along x-axis.	34
Figure 14. Δ CFF contoured in the fault plane of the SCRf and the SSVFC for 50 year scenario. Distance increases southward along x-axis.	35
Figure 15. Δ CFF contoured in the fault plane of the SCRf and the SSVFC for 100 year scenario. Distance increases southward along x-axis.	36
Figure 16. Δ CFF profile at 5 km depth along SCRf and SSVFZ. The dashed red line marks the 10 kPa value, which is used as a static stress triggering threshold. Values above this line represent greater risk of fault rupture.	37
Figure 17. Δ CFF in plane of Schell Creek Range fault and Southern Spring Valley fault zone under the assumption of a vertical fault with purely dextral (right-lateral) motion for the 100 year pumping scenario. When compared with the normal-motion scenario, the Δ CFF here is much less. The Δ CFF did not reach above the 10 kPa threshold in either the 10 year, 50 year, or 100 year scenarios.	38
Figure 18. Δ CFF cross section at 5 km depth from the plane of the Schell Creek Range fault and Southern Spring Valley fault zone under the assumption of purely dextral (right-lateral) motion for the 10, 50, and 100 year pumping scenario. No transient pumping scenarios showed enough Δ CFF increase to surpass the 10 kPa threshold.	39
Figure 19. Comparison of Δ CFF ranges for hydrologic mass unloading with the Spring Valley pumping scenarios (10 year, 50 year, and 100 year).....	42

Introduction

Addition or removal of a load on the Earth's surface alters the state of stress in the subsurface (Boussinesq, 1885; Farrell, 1972; Love, 1929). The resulting stress change has potential to unclamp faults locked under the regional tectonic stress resulting in short-term slip-rate increases (Hetzel & Hampel, 2005) or, in some cases, can trigger rupture on faults (Gonzalez, Tiampo, Palano, Cannavo, & Fernandez, 2012). Significant crustal surface-load removal can result from hydrospheric mass changes, such as groundwater pumping and transfer. This study introduces a method to rapidly evaluate the susceptibility of faults to rupture or slip-rate increase due to large-scale hydrologic mass changes from groundwater pumping.

Mechanics of stress transfer/stress change

The earth's crust exhibits elastic behavior under a wide range of forces (Turcotte & Schubert, 2002). That is, when the crust is deformed under a load, it will return to its original shape when the load is removed. The stick-slip pattern of motion along a fault is an effect of this elastic behavior, and to first order, results from two opposing forces. Tectonic forces create shear stress in a fault plane and drive motion along the fault. The shear stress is opposed by the frictional strength of the fault, which is a function of the normal stress acting on the fault and the frictional resistance of the fault to motion (Jaeger, Cook, & Zimmerman, 2007; Twiss & Moores, 1992). The elastic nature of the crust allows shear stress to accumulate over time in response to tectonic forcing. Failure occurs on a fault plane when the shear stress reaches the magnitude of the frictional strength of the fault. This relationship is known as the Coulomb failure criterion (Jaeger et al., 2007; Twiss & Moores, 1992):

$$(1) \quad |\tau| = s + \mu_f(\sigma_n),$$

where τ is the shear stress, μ_f is the coefficient of friction (a material property), σ_n is the stress normal to the plane, and s is material cohesion. The normal stress is typically a function of the lithostatic stress acting on the fault, and the presence of pore-water in porous media effects the stress state as if the confining pressure were lowered by an amount equal to the pore-water pressure. This reduction in the stress state is known as effective stress (Twiss & Moores, 1992). By the Coulomb failure criterion (equation 1(2) σ_c), the Coulomb stress is expressed by the Coulomb failure function (CFF):

$$(2) \quad \sigma_c = \tau_s - \mu_f(\sigma_n - p) + s,$$

where σ_c is the Coulomb stress, τ_s is the shear stress on the fault, and p is pore pressure. When the strength of the fault, $\mu_f(\sigma_n - p) + s$, is greater than the shear stress, τ_s , the value is negative and the fault is locked, accumulating elastic strain over time. When the shear stress is greater than the strength of the fault, the Coulomb stress is positive and can result in an earthquake by fault rupture and release of accumulated elastic strain. A decrease in normal stress can unclamp the fault, which allows failure at lower levels of shear stress. Fault failure can be due to an increase in pore pressure that reduces the effective normal stress on a fault or due to a change in either normal stress or shear stress by mechanical means (Ellsworth, 2013; McGarr, Simpson, & Seeber, 2002).

Over longer time scales or under the influence of larger loads, the crust may respond viscoelastically; the crust will initially deform elastically, but over time, it relaxes under elastic strain and begins to deform permanently (Turcotte & Schubert, 2002). Displacement from this

relaxation following earthquakes in the Great Basin has been observed within multi-decadal time scales (Gourmelen & Amelung, 2005).

Background (previous studies)

Naturally occurring hydrologic crustal loading cycles have been implicated in altering fault slip-rates and affecting seismicity patterns (Bettinelli et al., 2008; Hetzel & Hampel, 2005). Examples of long-term loading-unloading cycles are glacial-interglacial cycles, growth and retreat of ice sheets, and filling and disappearance of large pluvial lakes such as Lake Bonneville and Lake Lahontan in the Great Basin or ancient Lake Cahuilla in southern California (Hampel, Hetzel, & Densmore, 2007; Hampel, Hetzel, & Maniatis, 2010; Hampel, Hetzel, Maniatis, & Karow, 2009; Hetzel & Hampel, 2005; Karow & Hampel, 2010; Luttrell, Sandwell, Smith-Konter, Bills, & Bock, 2007; Turpeinen, Hampel, Karow, & Maniatis, 2008).

Figure 1 below includes a schematic from Hampel and Hetzel (2006) that illustrates the stress changes resulting from loading / unloading cycles using the Mohr circle diagram representation of stress at a point in the subsurface. The Mohr diagram uses axes of normal stress (horizontal axis) vs shear stress (vertical axis) with maximum and minimum principal stresses plotted on horizontal axis. The center of the circle is the average of the maximum and minimum principal stresses, and the diameter is the differential stress. Plane orientation in the subsurface is represented by points on the circle, and thus normal and shear stress on the fault plane can be read from the plot as long as the maximum and minimum principal stresses are known.

Hydrologic loading, such as filling of lakes or growth of ice sheets, causes deformation of the crust and an increase in normal stress on faults in the crust near or beneath large loads. An

increase in normal stress causes a clamping effect resulting in a decrease in rate of displacement along the fault and thus a decrease in earthquake frequency (Hampel & Hetzel, 2006). During this time of seismic quiescence, elastic strain continues to accumulate due to unchanged tectonic driving forces. When the local load is removed, the accumulated elastic strain can be released, resulting in an increase in displacement at the fault and increased earthquake occurrence (Hampel & Hetzel, 2006; Hetzel & Hampel, 2005). During loading of the crust, both the maximum and minimum principal stresses are increased, which brings the stress state farther from failure, or in essence, clamping the fault shut. When unloading occurs, maximum and minimum principal stresses are decreased toward failure again (**Figure 1**).

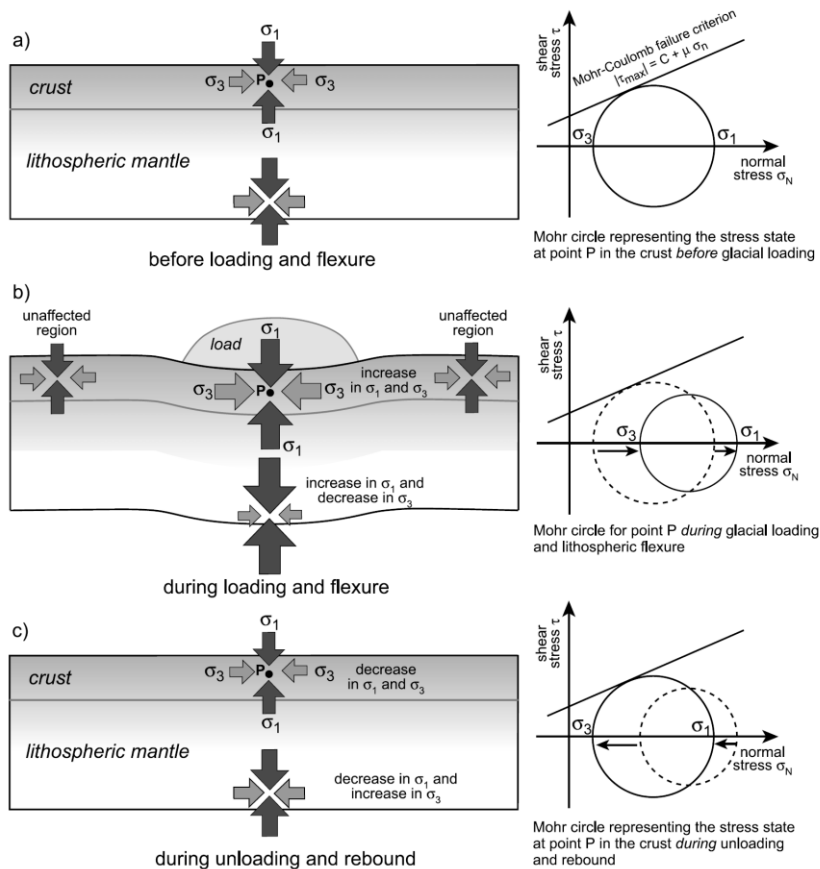


Figure 1. Mohr circle diagram of stress change from loading/unloading cycles. Before loading, the stress state in the crust is near failure (*from* Hampel & Hetzel, 2006).

In the case of the draining of Lake Cahuilla, induced elastic flexure of the crust perturbed stress regimes on the proximal San Andreas and San Jacinto strike-slip faults enough to be implicated in modulating temporal seismicity patterns (Luttrell et al., 2007). Elastic flexure of the crust beneath the lake created horizontal compressive forces during loading and extensional forces when the load was removed. Outside the lake loading area, horizontal compressive forces were reduced during loading to accommodate downward flexure beneath the load, and horizontal compressional forces were increased during unloading as the crust rebounded. Depending on the position of the fault with respect to the lake, the San Andreas and San Jacinto faults were either clamped or unclamped during unloading periods. The resulting change in Coulomb stress from these loading cycles was estimated to be in the range of 100 – 200 kilopascals (kPa) during unclamping, which likely drove the fault to failure (Luttrell et al., 2007).

Similar patterns of cyclic loading from annual hydrologic variations have also been linked by statistical methods to seasonal patterns of seismicity and uplift in tectonically active areas such as Japan, California, and the Himalaya (Bettinelli et al., 2008; Christiansen, Hurwitz, & Ingebritsen, 2007; Heki, 2003). Annual hydrologic variation in the Himalaya region was estimated to induce a 2-4 kPa change in Coulomb stress on the nearby Himalayan thrust, although correlation of seismicity occurrence was best with rate of stress change rather than magnitude of stress changes (Bettinelli et al., 2008). An increase in rate of stress change as a driver of seismicity has been observed previously in an instance of dike intrusion in Japan (Toda, Stein, & Sagiya, 2002). During dike intrusion, stressing rate was increased 1,500 fold from the

secular rate, and strong spatial and temporal correlations were drawn between earthquake occurrence and rate of stress change (Toda et al., 2002).

Several anthropogenically triggered earthquakes have been described (Costain and Bollinger, 2010; Ellsworth, 2013; McGarr et al., 2002) as human modifications to the hydrosphere have reached scales of unloading sufficient to incur a crustal response similar to natural unloading processes. Aquifers have historically been overexploited in places such as central California, southern Spain, and northern India. Mass removal in these areas has amounted to approximately 160 km³ in California over the past 150 years (Amos et al., 2014), approximately 20 km³ in southern Spain since the 1960s (Gonzalez et al., 2012), and roughly 1,240 km³ in northern India since the early 1970s (Kundu, Vissa, & Gahalaut, 2015). Approximate unloading volumes of ancient water bodies such as Lake Bonneville, Lake Lahontan, and Lake Cahuilla amount to 10,420 km³ (Karow & Hampel, 2010), 2,020 km³ (Karow & Hampel, 2010), and 810 km³ (Luttrell et al., 2007), respectively. While these lake volumes are greater than modern groundwater pumping amounts, the average area over which the pluvial lakes have retreated is much larger than the zone of influence for groundwater pumping. For example, the area of ancient Lake Bonneville amounted to approximately 52,568 km² (Karow & Hampel, 2010), whereas the size of the entire Alta-Guadalupe basin in southern Spain is approximately 80 km² (Gonzalez et al., 2012). A cursory comparison of average pressure acting near the surface from load removal is similar, with 2.29×10^3 kPa resulting from the retreat of Lake Bonneville, and 2.45×10^3 kPa resulting from groundwater pumping in southern Spain.

Primary influencing factors observed in cases of seismicity occurrence and fault slip-rate increases are the magnitude of surface load changes (Hampel & Hetzel, 2006) and the rate of stress change (Bettinelli et al., 2008; Toda et al., 2002). Because change in fault-normal stress is

the influencing parameter on fault failure (**equations 1 & 2**), comparison of stress values is more appropriate than comparison of a change in load mass. **Figure 2** shows the change in surface pressure $\left(\frac{\Delta Load}{\Delta Area}\right) = \Delta\sigma$ versus average rate of surface pressure change $\Delta\sigma/\Delta t =$ rate of stress change for reported instances of unloading-related fault ruptures or slip-rate increases. The comparison highlights where 1) stressing rate may be the driver of increasing seismicity, 2) the magnitude of the load change is the driver, or 3) seismicity *is* driven by a combination of stressing rate and load change magnitude. Just as retreat of glaciers or regression and disappearance of large pluvial lakes have been shown to alter subsurface stress and fault slip rates, high-volume pumping of groundwater basins creates similar crustal-stress perturbations that can induce uplift and decrease normal stress on nearby faults (Amos et al., 2014; Gonzalez et al., 2012; Trugman, Borsa, & Sandwell, 2014).

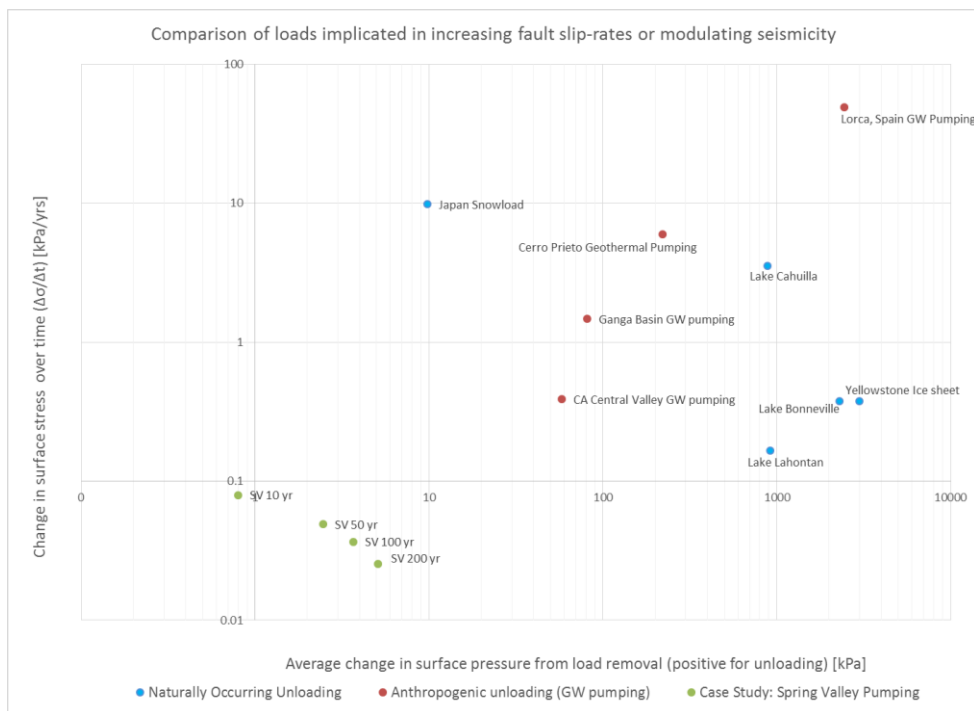


Figure 2. Rate of surface stress change $\left(\frac{\Delta\sigma}{\Delta t}\right)$ versus the change in surface stress for a variety of natural and anthropogenic crustal unloading events.

Lorca, Spain groundwater pumping has a similar surface pressure response to Lake Bonneville and the ancient Yellowstone ice sheet, although the Lorca, Spain groundwater pumping has a much higher stressing rate. Conversely, groundwater pumping in the Central Valley of California has a similar annual unloading rate as both Lake Bonneville and the ancient Yellowstone ice sheet, though the average surface pressure change from pumping in California is much lower. This does not account for the distance between faults and the unloading area, thus relationships may not translate into change in Coulomb stress activated on nearby faults. Actual fault rupture potential is controlled by Coulomb stress change (**equation 2**), as we discuss below.

Previous study methods

The impact of long-term surface loading cycles on proximal faults can be simulated using finite-element numerical models of an elasto-plastic crust and an elasto-visco-plastic lithospheric mantle with the effects of rheological parameters such as density, Young's modulus, viscosity, and secular tectonic velocity. In cases of large load changes taking place on time scales of 10^3 - 10^4 years spread over large areas of the crust (e.g. formation and disappearance of Lake Bonneville or the Yellowstone ice sheet), the viscoelastic response of the deep crust and upper mantle is likely to have a significant effect on stress loading patterns on proximal faults (Hampel & Hetzel, 2006; Hampel et al., 2010; Hetzel & Hampel, 2005). Models of loads on this scale over a purely elastic crust suggest behavior opposite of those which account only for viscoelastic effects (Hampel & Hetzel, 2006).

Despite this difference, the infinite elastic crust assumption is used when surface loads are relatively small because governing equations have three dimensional (3D) analytic and semi-

analytic solutions for resolution of the full 3D stress tensor from the application of a point-load (Boussinesq, 1885), rectangular-shaped load (Love, 1929), or circular-shaped load (Love, 1929), and has proven useful when surface loads are relatively small (Bettinelli et al., 2008; Luttrell et al., 2007). These solutions, which have variations for both stress and deformation, ignore the effects of the viscoelastic behavior of the crust and thus are most effective for loads of smaller magnitude acting over shorter time scales. For example, deformation resulting from the annual variations of water storage in the Ganges basin have been simulated using both finite element analysis with consideration of an elastic plate overlying a non-viscous fluid as well as by use of the simplified analytical solutions of Boussinesq (1885) (Bettinelli et al., 2008). Results from both of the models, despite different assumptions on the behavior of the crust, matched geodetic observations remarkably well (Bettinelli et al., 2008).

Solutions developed from Boussinesq's (1885) solution were for a homogenous, isotropic, semi-infinite half space and similar solutions have been developed using different assumptions such as the response from a static load under assumption of a spherical, radially stratified, gravitating earth (Farrell, 1972).

Resolving a change in CFF on faults near the source of unloading is a common approach to determine the likelihood of increased risk of fault rupture. Two-dimensional (2D) models that conceptualize subsurface stress as an infinite rectangular line-load with a finite width over a purely elastic infinite half-space have been used to evaluate stress changes from pumping in the Central Valley of California (Amos et al., 2014) and from the influence of pumping in the Ganga basin on the MHT (Kundu et al., 2015). In the case of central California, uplift was also modeled using a Boussinesq-based analytical displacement solution for comparison with observed geodetic data. Using mass of hydrologic-unloading determined from Gravity Recovery and

Climate Experiment (GRACE) data, modeled uplift was observed to correspond with uplift recorded by continuous global positioning system (GPS) stations. The resulting conclusions were that water withdrawal in the California Central Valley was causing crustal rebound (Amos et al., 2014).

Shallow pumping / shallow drawdown (relative to seismogenic depths)

Fault ruptures causing earthquakes typically originate between 6-15 kilometers (km) deep in the crust (Jackson, 1987), and this region is known as the seismogenic zone.

Groundwater pumping for municipal, industrial, or agricultural use typically occurs several kilometers above the seismogenic zone. Because of this, the pore-pressure on the fault at seismogenic depth is often unaffected by pumping and the driver of the change in CFF is a mechanical reduction in normal stress due to load removal (**Figure 3**). To calculate the change in Coulomb failure function stress (ΔCFF) resulting only from a shear stress or normal stress change, the pore-pressure and material cohesion terms from equation 2 are assumed constant:

$$(3) \quad \Delta\sigma_c = \Delta\tau_s + \mu_f\Delta\sigma_n$$

To quantify the tendency of the fault toward failure, the sign convention in equation 3 is different from that in equation 2. A shear stress change toward failure (in favor of tectonic motion) is positive, while a normal stress change that unclamps the fault is also positive (King, Stein, & Lin, 1994; Stein, 1999). Under this convention, a greater value of ΔCFF will signify greater likelihood of failure. The increased likelihood of failure resulting from load removal is driven by the combination of decreased normal stress and increased shear stress. Their relative weight depends on the geometry and orientation of the fault with respect to the load removal.

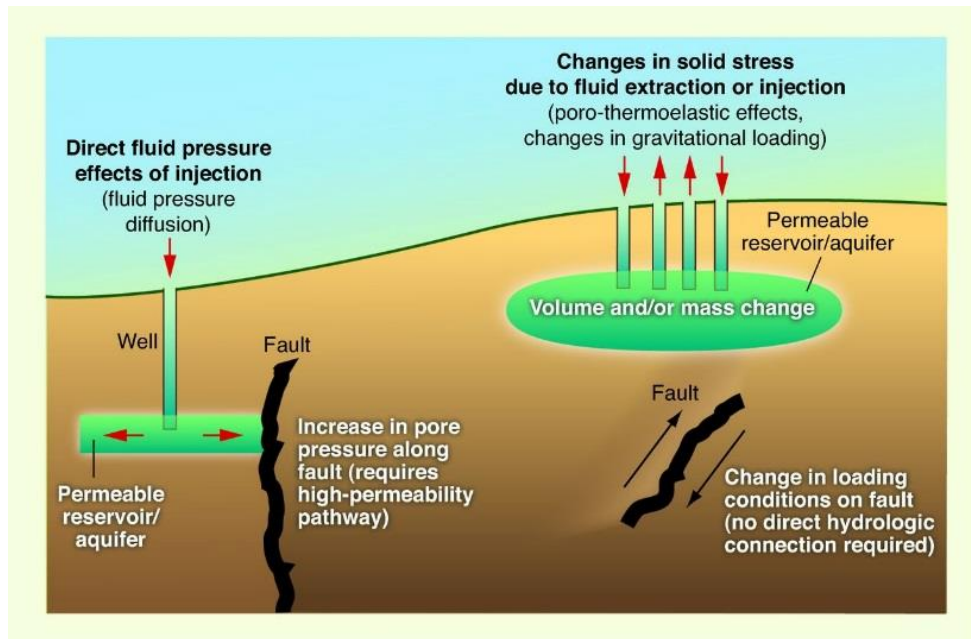


Figure 3. Schematic diagram of mechanisms for inducing earthquakes. Earthquakes may be induced by increasing the pore pressure acting on a fault (**left**) or by changing the shear and normal stress acting on the fault (**right**) (from Ellsworth, 2013).

Fault Rupture Triggering Thresholds

The subsurface state of stress on faults at seismogenic depth is close to the strength of the fault, even in stable intraplate areas (Grasso & Sornette, 1998; Townend & Zoback, 2000; Zoback & Harjes, 1997). This means that only a small ΔCFF increase has potential to bring a fault to failure. The critical ΔCFF is a function of the proximity of the fault to failure, and earthquakes themselves have given clues to this magnitude. Large earthquakes release stress on a source fault, altering stress on surrounding faults (Stein, 1999). Correlation of spatial patterns of static stress increases in the crust with locations of aftershocks have revealed ‘triggering thresholds’, or subsurface static stress changes above which there is a higher frequency of aftershock occurrence (Anderson & Johnson, 1999; Hardebeck, Nazareth, & Hauksson, 1998; King et al., 1994; Lockner & Beeler, 1999; Reasenber & Simpson, 1992). ΔCFF of 10 kPa (0.01 megapascals (MPa) or 0.1 bar) marks the boundary between low and high correlation with aftershock

occurrence (Anderson & Johnson, 1999). Fault stress changes above 10 kPa represent a likely chance of failure and earthquakes.

Δ CFF for several notable pumping-induced failure events was observed to approach or exceed 10 kPa (**Table 1**). Subsurface stress change due to groundwater pumping in the Alto Guadalentin Basin in Spain has been connected to the coseismic fault slip distribution of the 2011 M_w 5.1 earthquake along the Alhama de Murcia fault in Lorca, Spain (Gonzalez et al., 2012). Groundwater pumping caused a stress change in the fault plane that is correlated with the location and progression of the fault slip during the event. Δ CFF on the fault plane in the location of largest slip magnitude was 5 kPa (0.05 bar) with slip progressing to areas of Δ CFF change of 10 kPa (0.1 bar). Similarly, the 2010 M_w 7.2 El Mayor-Cucapah (EMC) earthquake that ruptured faults in Northern Baja California into southern California correlates with a subsurface stress change due to pumping in the nearby Cerro Prieto Geothermal field (Trugman et al., 2014). Pumping in the geothermal field added 15 kPa/yr (0.15 bar/yr) of positive Coulomb stress near the hypocenter of the EMC rupture. Agricultural groundwater pumping in the Indo-Gangetic plains has likewise been implicated in the 2015 M_w 7.8 Gorkha, Nepal earthquake. The Gorkha earthquake is reported to have been along the MHT, which lies adjacent to the Indo-Gangetic plains and its corresponding aquifers (Kundu et al., 2015). The enhancement of Coulomb stress on the locked portion of the MHT due to pumping from the Ganga basin aquifer has been approximated to be 3-8 kPa (0.03-0.08 bar) since pumping began roughly 55 years ago. Finally, groundwater pumping in California's Central Valley is likely a contributor to the modulation of seismic activity on both the San Andreas Fault and the Coalinga thrust in central California (Amos et al., 2014). The stress increase from groundwater depletion in the San Joaquin Valley since the late 1800s has contributed an estimated stress change of 2.7-9.5 kPa

(0.027 – 0.095 bar) Δ CFF to the nearby San Andreas Fault, and 10-15 kPa (0.10 – 0.15 bar) on the nearby Coalinga thrust.

Table 1. Comparison of studies implicating groundwater pumping as cause of earthquake rupture						
Reference	Fault type	Unloading Source	Unloading Volume	Unloading Area	Unloading Time Period	ΔCFF on applicable fault(s)
Gonzalez et al.	Strike Slip - rake = 36°	Agricultural GW pumping in Alto-Guadelentin basin	20 km ³	80 km ²	50 yrs	5-10 kPa
Trugman et al.	Strike Slip	Cerro Prieto Geothermal Field	0.36 km ³	16 km ²	~37 yrs	10-15 kPa
Kundu et al.	Thrust	Agricultural GW pumping from Indo-Gangetic Plains	1240 km ³	1.5e5 km ²	~55 yrs	3-8 kPa
Amos et al.	Strike Slip (San Andreas)	California Central Valley (San Joaquin Basin)	160 km ³	27,000 km ²	~150 yrs	2.7-9.5 kPa
Amos et al.	Thrust (Coalinga)	California Central Valley (San Joaquin Basin)	160 km ³	27,000 km ²	~150 yrs	10-15 kPa

Both the consistency of these values between multiple studies [Anderson and Johnson, 1999; King et al., 1994; Lockner and Beeler, 1999; Reasenber and Simpson, 1992] and the observations of Δ CFF values from instances of earthquakes triggered by groundwater pumping (Table 1) support this value for our application. We conservatively choose the same threshold (10 kPa or 0.1 bar) to mark the lower end of the Δ CFF range for potential danger of fault failure in future large-scale groundwater pumping scenarios. However, this threshold does not guarantee a fault rupture, thus the value is used as a “danger zone” threshold, where a Δ CFF of this magnitude puts the fault in a category of a potential failure.

Methods

Large-scale groundwater withdrawal can increase seismic activity or trigger seismic rupture on a fault. Here we present methods for calculating normal and shear stress acting on a fault in an elastic crust based on both 2D and 3D analytical solutions by incorporating 3D numerical groundwater models that estimate the spatial distribution of unloading due to pumping. This method assumes elastic behavior of the crust, which assumption holds for shorter time scales and surface load changes that do not induce significant amounts of crustal flexure (Bettinelli et al., 2008). While viscoelastic deformation has been observed in the Great Basin on time scales as short as several decades (Gourmelen & Amelung, 2005), deformation is minimal, and continuing deformation signifies the remaining presence of elastic strain in the crust. Also, elastic strain continues to accumulate on faults in the Great Basin over time scales of 10^3 years as evidenced by recurrence intervals (Hammond, Blewitt, & Kreemer, 2014; Koehler & Wesnousky, 2011), thus crustal response to surface load changes occurring over multi-decadal to single century time scales are assumed sufficiently modeled by elastic behavior as well.

Static stress change modeling using the assumption of a two-dimensional (2D) surface load

Analytical solutions typically used in rock mechanics and geotechnical engineering applications exist to resolve subsurface stress in an elastic half-space resulting from a simplified 2D surface load, such as a uniform disc or an infinite rectangular line-load (Boussinesq, 1885; Jaeger et al., 2007). For example, if mass removed can be represented by an infinite rectangular line load, the stress at the point (X_0, Z_0) can be resolved using the assumption of geometry shown on **Figure 4** (Jaeger et al., 2007):

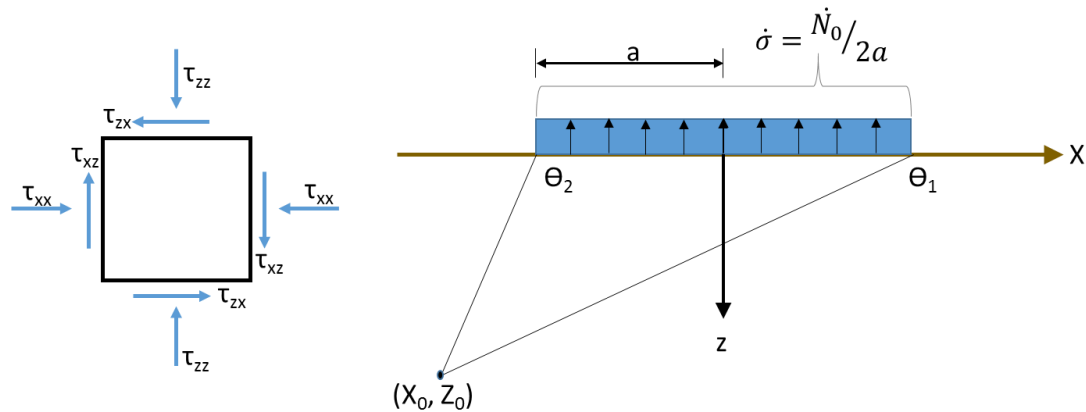


Figure 4. Geometry and sense of stress for two-dimensional subsurface stress modeling equations after Jaeger et al. (2007).

' N_0 ' is the load [force], ' a ' is the half-width of the line-load [length], and the angles ' θ_1 ' and ' θ_2 ' are measured clockwise from the surface at the right and left load edges, respectively (**Figure 4**).

The resulting stress at (X_0, Z_0) is:

$$(4) \quad \tau_{xx} = \frac{N_0}{2\pi a} [(\theta_1 - \theta_2) + \sin(\theta_1 - \theta_2) \cos(\theta_1 + \theta_2)]$$

$$(5) \quad \tau_{zz} = \frac{N_0}{2\pi a} [(\theta_1 - \theta_2) - \sin(\theta_1 - \theta_2) \cos(\theta_1 + \theta_2)]$$

$$(6) \quad \tau_{xz} = \frac{N_0}{2\pi a} [\sin(\theta_1 - \theta_2) \sin(\theta_1 + \theta_2)]$$

The normal (σ_n) and shear (τ_s) stress acting on a plane with a dip angle ϕ from horizontal can then be calculated:

$$(7) \quad \sigma_n = \tau_{zz} \cos^2(\phi) - 2\tau_{xz} \sin(\phi) \cos(\phi) + \tau_{xx} \sin^2(\phi)$$

$$(8) \quad \tau_s = (\tau_{zz} - \tau_{xx}) \sin(\phi) \cos(\phi) + \tau_{xz} (\cos^2(\phi) - \sin^2(\phi)).$$

These solutions account for one dimension (N-S, E-W, etc.), modeled as X, and depth modeled as Z.

3D static stress change modeling using groundwater modeling

An industry standard in groundwater modeling is MODFLOW, which is a finite-difference block-centered groundwater flow modeling approach that solves the groundwater-flow equation (equation 9):

$$(9) \quad \frac{\partial}{\partial x} \left[K_{xx} \frac{\partial h}{\partial x} \right] + \frac{\partial}{\partial y} \left[K_{yy} \frac{\partial h}{\partial y} \right] + \frac{\partial}{\partial z} \left[K_{zz} \frac{\partial h}{\partial z} \right] + W = S_s \frac{\partial h}{\partial t}$$

where K_{xx} , K_{yy} , and K_{zz} , are values of hydraulic conductivity aligned with the x, y, and z axes. h is the potentiometric head, W represents sources and/or sinks of water as a volumetric flux, S_s is the specific storage (for a confined system), and t is time (Harbaugh, Banta, Hill, & McDonald, 2000). In an unconfined system such as the one used for the case study in this work, S_s is replaced with S_y , for specific yield. In a confined system the water lost from the aquifer is due to both elastic expansion of water and contraction of the aquifer, which is quantified by specific storage S_s . In an unconfined system the water lost is due to water drainage from pore space in the porous media, which is quantified for a given volume as a ratio of the volume of drained water to the total volume.

MODFLOW is a platform that allows a user to combine multiple modules that simulate different aspects of the subsurface hydrologic cycle (Harbaugh et al., 2000), including influx of water into the system in the form of precipitation, specified-flux boundaries, rivers & streams, etc., as well as out-flux through sinks such as evapotranspiration (ET), pumping wells, specified-flux boundary conditions, streams & springs, etc. Flow can then be modeled by solving equation 9 at each grid node with consideration of influxes, out-fluxes, boundary conditions (i.e. Dirichlet,

or specified-head conditions; Neumann, or specified-flux boundaries; Cauchy, or head-dependent boundaries), as well as horizontal or vertical flow barriers and other modules available through MODFLOW. MODFLOW can be used for a steady-state simulation considering inputs and outputs to the model or for transient simulations over a specified time period. The output from transient simulations includes potentiometric head (and thus, drawdown) and flow across specified boundaries. Planning for large-scale groundwater extraction projects often includes development of transient groundwater models.

Drawdown data from groundwater models can be used for estimation of static-stress change in the subsurface. Import and export data from a groundwater model typically has 3D grid structure. The equivalent force N_i generated by changing mass of each grid cell i is calculated using

$$(10) \quad N_i = (\text{area}_i) \times (\text{drawdown}_i) \times (\text{specific yield}_i) \times \rho \times g,$$

where ρ is water density and g is gravity (1,000 kg/m³ and 9.81 m/s², respectively). Each point load (N_i) exerts stress on nodes directly beneath itself and also on surrounding nodes as well. Thus, the stress change from cells with drawdown in the grid must be resolved at every cell across the grid. By the principle of superposition, the effect of the force exerted by all other cells can be summed to resolve the cumulative state of stress at any point (Jaeger et al., 2007). We assume that the force at each cell can be approximated as a point when calculating stress at a large distance ($r = \sqrt{x^2 + y^2 + z^2}$). The components of the three-dimensional symmetric stress tensor

$$\begin{bmatrix} \tau_{xx} & \tau_{xy} & \tau_{xz} \\ \tau_{yx} & \tau_{yy} & \tau_{yz} \\ \tau_{zx} & \tau_{zy} & \tau_{zz} \end{bmatrix} = \begin{bmatrix} \tau_{xx} & \tau_{xy} & \tau_{xz} \\ \tau_{xy} & \tau_{yy} & \tau_{yz} \\ \tau_{xz} & \tau_{yz} & \tau_{zz} \end{bmatrix}$$

at a point in a homogenous, isotropic, elastic, half-space resulting from a point-load at the surface of the half-space can be computed by

$$(11) \quad \tau_{xx} = \frac{N_i}{2\pi} \left[\frac{3x^2z}{r^5} + \frac{(1-2\nu)(y^2+z^2)}{r^3(z+r)} - \frac{(1-2\nu)z}{r^3} - \frac{(1-2\nu)x^2}{r^2(z+r)^2} \right]$$

$$(12) \quad \tau_{yy} = \frac{N_i}{2\pi} \left[\frac{3y^2z}{r^5} + \frac{(1-2\nu)(x^2+z^2)}{r^3(z+r)} - \frac{(1-2\nu)z}{r^3} - \frac{(1-2\nu)y^2}{r^2(z+r)^2} \right]$$

$$(13) \quad \tau_{zz} = \frac{N_i}{2\pi} \left[\frac{3z^3}{r^5} \right]$$

$$(14) \quad \tau_{xy} = \frac{N_i}{2\pi} \left[\frac{3xyz}{r^5} - \frac{(1-2\nu)xy(z+2r)}{r^3(z+r)^2} \right]$$

$$(15) \quad \tau_{yz} = \frac{N_i}{2\pi} \left[\frac{3yz^2}{r^5} \right]$$

$$(16) \quad \tau_{xz} = \frac{N_i}{2\pi} \left[\frac{3xz^2}{r^5} \right]$$

where ν is the Poisson's ratio of the material which describes the proportional ratio of lateral contraction to an increase in length of a material that is elastically stretched (Jaeger et al., 2007). The spatial representation of each component is shown on **Figure 11**.

The resolution of the stress tensor allows for an accounting of the complete change in the state of stress in the subsurface as a result of pumping. If the orientation of the force/stress grid is not aligned with the strike and dip of the fault, the stress tensor must undergo coordinate transformation to properly distinguish normal and shear stress acting on the fault plane.

Coordinate rotation for a three dimensional tensor is computed using

$$(17) \quad T' = L T L^T$$

where T' is the transformed matrix, T is the original matrix, L is the transformation matrix, and L^T is the transpose of the transformation matrix (Jaeger et al., 2007). For rotation around the x-axis

$$L_x = \begin{bmatrix} 0 & 0 & 0 \\ 0 & \cos\theta & \sin\theta \\ 0 & -\sin\theta & \cos\theta \end{bmatrix}; \text{ for rotation around the y-axis, } L_y = \begin{bmatrix} \cos\theta & 0 & \sin\theta \\ 0 & 0 & 0 \\ -\sin\theta & 0 & \cos\theta \end{bmatrix};$$

and for rotation around the z-axis, $L_z = \begin{bmatrix} \cos\theta & \sin\theta & 0 \\ \sin\theta & \cos\theta & 0 \\ 0 & 0 & 0 \end{bmatrix}$.

The shear and normal components of stress change acting in the fault plane can then be read from the transformed stress tensor. The component corresponding to the direction of shear along the fault is used as the change in shear stress, and the component normal to the fault plane describes the change in normal stress. The normal and shear stress are then used as input for equation 3 to resolve the ΔCFF . The ΔCFF can then be compared with static stress change triggering thresholds to determine if the fault is at increased risk of rupture.

Case Study: Spring Valley

Persistent drought along with increasing population in southern Nevada has required the greater Las Vegas area to look for additional resources to supplement its water supply from the Colorado River. Permits have been granted by the Office of the State Engineer of Nevada for municipal-use groundwater rights in the eastern Nevada basins of Spring Valley, Cave Valley, Dry Lake Valley, and Delamar valley. The largest allocation is $75.4 \times 10^6 \text{ m}^3/\text{year}$ ($\sim 61,127$ acre-feet/year) from Spring Valley [SNWA[35], 2011] for transfer via pipeline from the northern valleys to Las Vegas. Like most Great Basin valleys, these valleys have bounding faults. A number of groundwater flow models have been developed for the area (Burns & Drici, 2011; Halford &

Plume, 2011; Myers, 2011; Prudic, Harrill, & Burbey, 1995). Faulting histories and tectonic strain constraints have also been developed for the area (Bennett, Wernicke, & Davis, 1998; Hammond et al., 2014; Koehler & Wesnousky, 2011).

At present, the seismic hazard of the central Great Basin is low due to low regional tectonic deformation rates ($\sim 1\text{-}2\text{mm/year}$) distributed across several range-bounding faults (Bennett, Wernicke, Niemi, Friedrich, & Davis, 2003; Hammond et al., 2014; Hammond & Thatcher, 2004). Consequently, most faults in the area are in a slip-rate class of <0.2 millimeters (mm) yr^{-1} (USGS & NBMG, 2016). In the following sections, we ask what ΔCFF will potentially be induced by pumping and how this compares with the ΔCFF thresholds discussed previously.

Spring Valley description

Spring Valley lies in the central Great Basin Province, which is characterized by widespread tectonic extension. Mountain ranges of the area are uplifted while basins are dropped by motion on normal faults accommodating the east-west extension. The Basin and Range province also accommodates shear resulting from the North American and Pacific plate boundary to the west (Hammond et al., 2014; Hammond & Thatcher, 2004). Spring Valley is a typical basin of the province as it is bounded by normal faults with a basin fill sediment aquifer reaching depths of a few kilometers (Welch, Bright, & Knochenmus, 2008).

The Spring Valley Hydrographic basin extends in a north-south direction approximately 240 km (150 miles) and is bounded by the Schell Creek Range on the west and the Snake Range on the east (**Figure 5**). The Antelope and Kern ranges bound the valley to the north with the Fortification Range extending along the southwestern flank. The highest peaks, and also the peaks that receive the most precipitation, are peaks such as Wheeler Peak (3,982 meters (m))

and Jeff Davis Peak (3,893 m) in the Snake Range and North Schell Peak (3,622 m) in the Schell Creek Range.

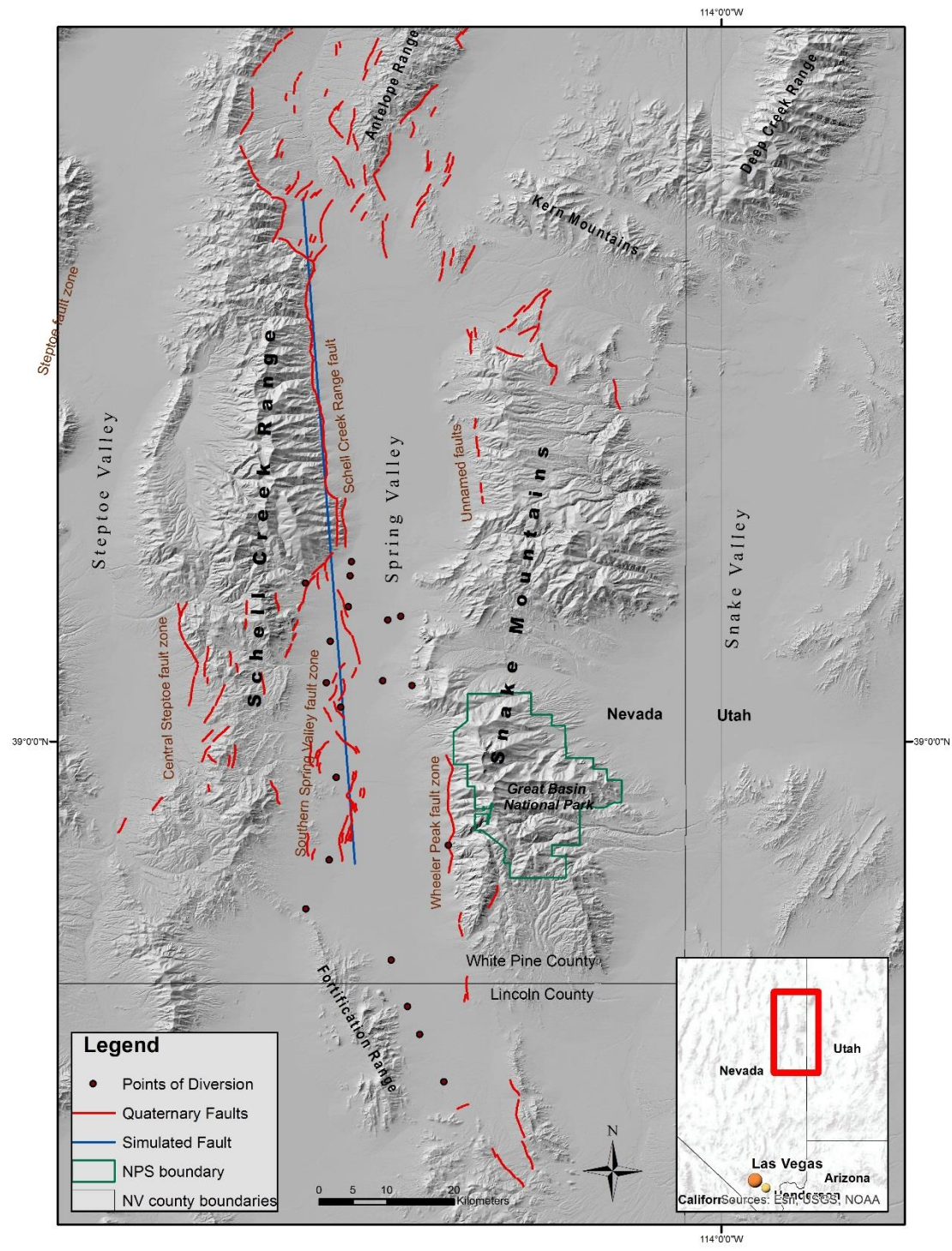


Figure 5. Spring Valley and surrounding ranges. Quaternary faults are shown in red as catalogued by the United States Geological Survey and the Nevada Bureau of Mines and Geology [USGS & NBMG, [45]2016]. Points of diversion corresponding to State-Engineer granted permits for municipal water use in the Las Vegas area are marked as points on the map.

In the central Great Basin region where Spring Valley lies, the subsurface has been separated into three main aquifer zones (Welch et al., 2008). The uppermost aquifer consists of basin fill sediments that are generally coarser toward the range fronts, and finer toward the centerline of the valleys. Beneath this system there is another water-bearing zone in the Tertiary volcanic strata (Welch et al., 2008). Beneath this lies a vast carbonate water bearing zone, known as the Basin and Range Carbonate Aquifer system. This lowest system is the purveyor of most inter-basin flow (Welch et al., 2008).

In Spring Valley, borehole records from an oil exploration well drilled in 1983 show that at one location near the center of the valley, the Cenozoic basin fill sediments extend to 1,097 m below ground surface (bgs) (Welch et al., 2008). Depths vary for the other water bearing regions, but as measured in the same borehole, the Cenozoic volcanics extended 375 m below the basin fill sediments, followed by 265 m of Tertiary sediments below that (Welch et al., 2008).

The points of diversion associated with the permits granted for groundwater withdrawal in Spring Valley are expected to have wells between 305 - 610 meters deep, and will mostly be drawing from the basin fill aquifer, with the possibility of some locations extending into the carbonate aquifer system based on location in the valley (SNWA, 2011).

Spring Valley Faults and tectonics

Spring Valley lies in the central great basin area in eastern Nevada's White Pine and Lincoln counties. The valley is a typical half-graben of the Great Basin geographic province and is bounded to the west by the Schell Creek Range and by the Snake Range to the east. The valley is being down dropped by normal motion on several faults that bound the valley.

Schell Creek Range fault

The Schell Creek fault is an east dipping range-front fault that marks the western boundary of Spring Valley. It is approximately 99 km in length striking roughly north-south and exhibits normal motion (Bartley & Wernicke, 1984; Depolo & Anderson, 2000; Dohrenwend, Schell, & Moring, 1991; Koehler & Wesnousky, 2011; Miller, Dumitru, Brown, & Gans, 1999). Paleoseismic analysis of a natural exposure near Piermont Creek has shown that there has been at least one, and possibly two seismic rupture events since around 30 ka, with a possibility of the latest event around 13 ka (Koehler & Wesnousky, 2011). Detailed analysis of rate of slip on this fault has not been completed, but remote analysis suggests a slip rate of close to 0.1 mm/year (Depolo & Anderson, 2000). The quaternary fault and fold database classifies this fault with a slip-rate of $<0.2 \text{ mm yr}^{-1}$ (USGS & NBMG, 2016). This fault is the largest in the basin and is the main focus of this study due to the size and identification of events on the fault.

Southern Spring Valley fault zone

The southern Spring Valley fault zone is a series of discontinuous faults that exhibit east-facing scarps in the Quaternary sediment of southern Spring Valley. These faults tend to splay basinward and to the south from the Schell Creek Range fault over a range of approximately 40 km and are likely synthetic faults expressing in the valley sediments (Depolo & Anderson, 2000;

Dohrenwend et al., 1991). The visible scarps in the area vary from 1-2 m in height, and are likely from a single event (Koehler & Wesnousky, 2011). The quaternary fault and fold database also classifies this fault with a slip-rate of $<0.2 \text{ mm yr}^{-1}$ (USGS & NBMG, 2016) . These faults are likely the most recent ruptures in the valley, so these will be considered in analysis as well.

Tectonics

Estimates of the Central Great Basin regional extension rate range from 1 mm/year (Koehler & Wesnousky, 2011) based on paleoseismic studies, fault diffusion analysis, and other methods based on geologic feature displacements to 1.9 mm/year (Bennett et al., 2003) and 2.0 mm/year (Hammond et al., 2014) based on continuous GPS data. The Schell Creek Fault and southern Spring Valley fault zone are the two most active fault traces (Koehler & Wesnousky, 2011), and these faults will be used as the focus of this analysis. The southern Spring Valley fault zone is modeled as an extension of the Schell Creek Range fault due to its location and similar strike (**Figure 5**).

Groundwater flow model description

Several groundwater models have been developed to simulate impact of groundwater pumping from Spring and Snake Valleys. The model used for the current study was developed by Halford and Plume (2011) for Great Basin National Park (GBNP) to resolve the timing and magnitude of water captured from nearby springs, streams, wetlands, and phreatophytes due to groundwater pumping in Snake Valley. The model was refined from the larger Great Basin Regional Aquifer-System Analysis model (RASA) (Prudic et al., 1995) excluding areas outside Spring and Snake Valleys. The grid cells are 12 km x 12 km near the outer portions of the model area, and the grid cell-size is progressively refined to 500 m x 500 m square cells in the area of interest around Great Basin National Park. The model was vertically divided into four layers; the

first layer accounts for groundwater-surface water interaction and was only 3.05 meters thick, the second layer was 15.25 meters thick to model fine-grained deposits, the third layer was to simulate basin fill greater than the thickness of layers one and two, and layer four simulated the basement rocks. The thickness of layers 3 and 4 was variable but summed to 610 meters. **Figure 6** shows a sample of model construction:

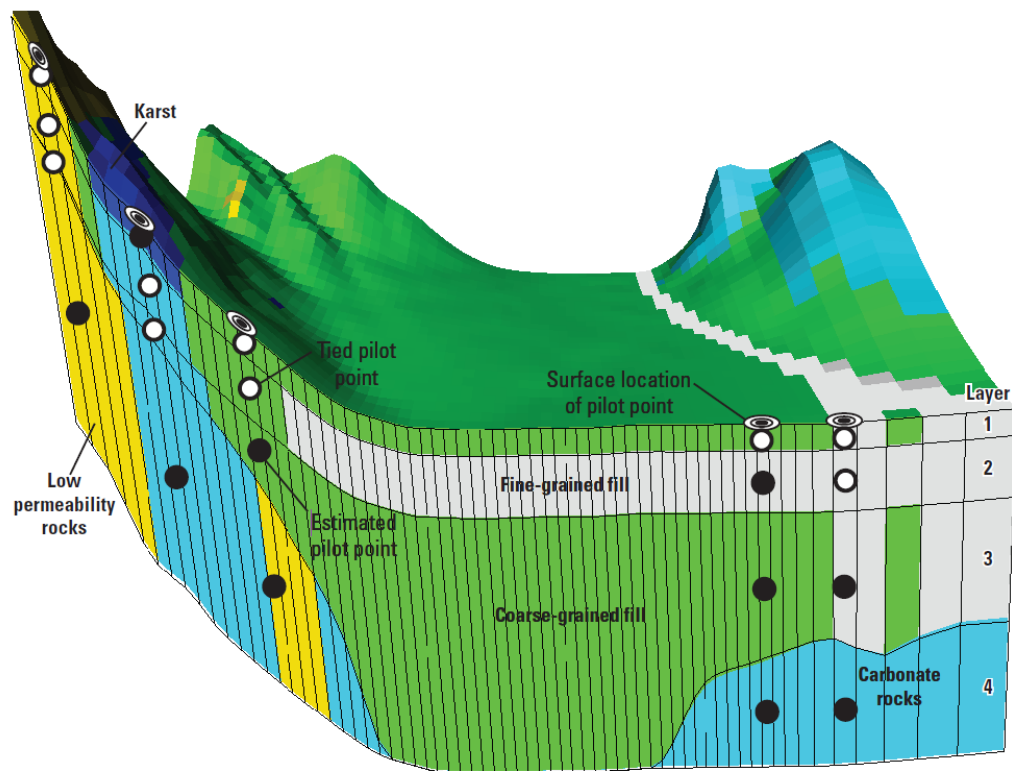


Figure 6. Sample model construction showing layers 1-4. Layer 1 is 3.05 m thick, layer 2 is 15.25 m thick, and layers 3 and 4 vary in thickness but do not exceed 610 m in thickness (*from Halford & Plume, 2011*).

The model was created using the direct drawdown approach, which uses both a calibration model and a separate predictive model. The calibration model was used to develop recharge and transmissivity distributions while the predictive model uses these transmissivity

distributions, estimates of specific yield, and groundwater discharges to model drawdown and capture of both distributed groundwater and spring discharges (Halford & Plume, 2011). In the calibration model, pilot points distributed throughout Spring and Snake Valleys were used to estimate recharge, hydraulic conductivity, and transmissivity parameters. These points were then interpolated with Kriging in areas with similar geology (Halford & Plume, 2011).

In the original model, points of diversion were limited to only nine wells in southern Snake Valley. For the current study, the wells in Snake Valley were replaced with 18 points of diversion in Spring Valley located in accordance with the permitted municipal use applications on file with the Nevada Division of Water Resources. These pumping wells were simulated with the multi-node well package in MODFLOW to simulate through multiple model layers. Results from this simulation are shown on **Figure 7**, **Figure 8**, and **Figure 9**:

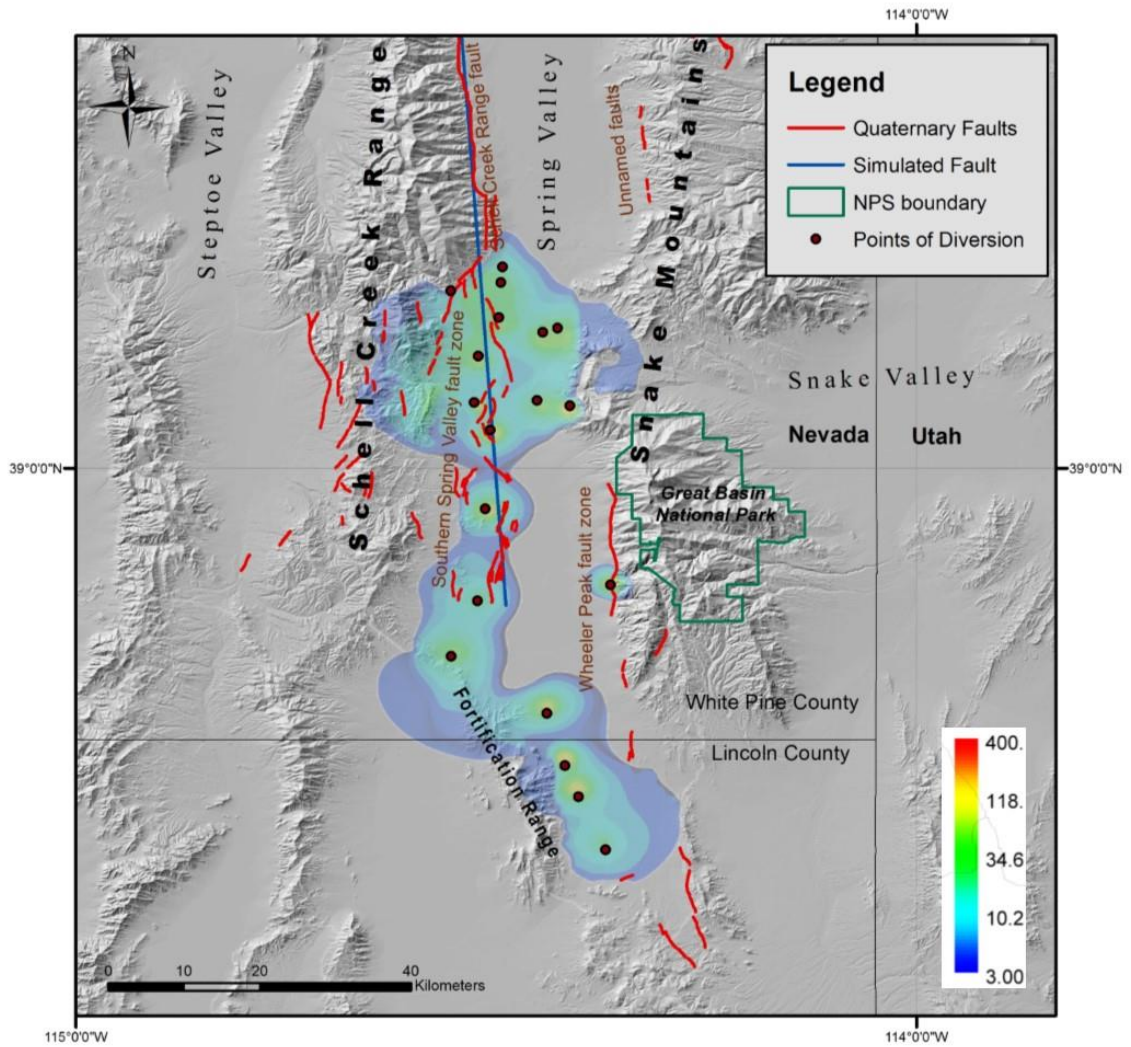


Figure 7. Drawdown (in feet) from pumping at a rate of $75.4 \times 10^6 \text{ m}^3/\text{year}$ ($\sim 61,127$ acre-feet/year) for 10 years from Halford & Plume (2011) with points of diversion modified to locations in accordance with the Office of the Nevada State Engineer applications 54003 to 54021 in Spring Valley.

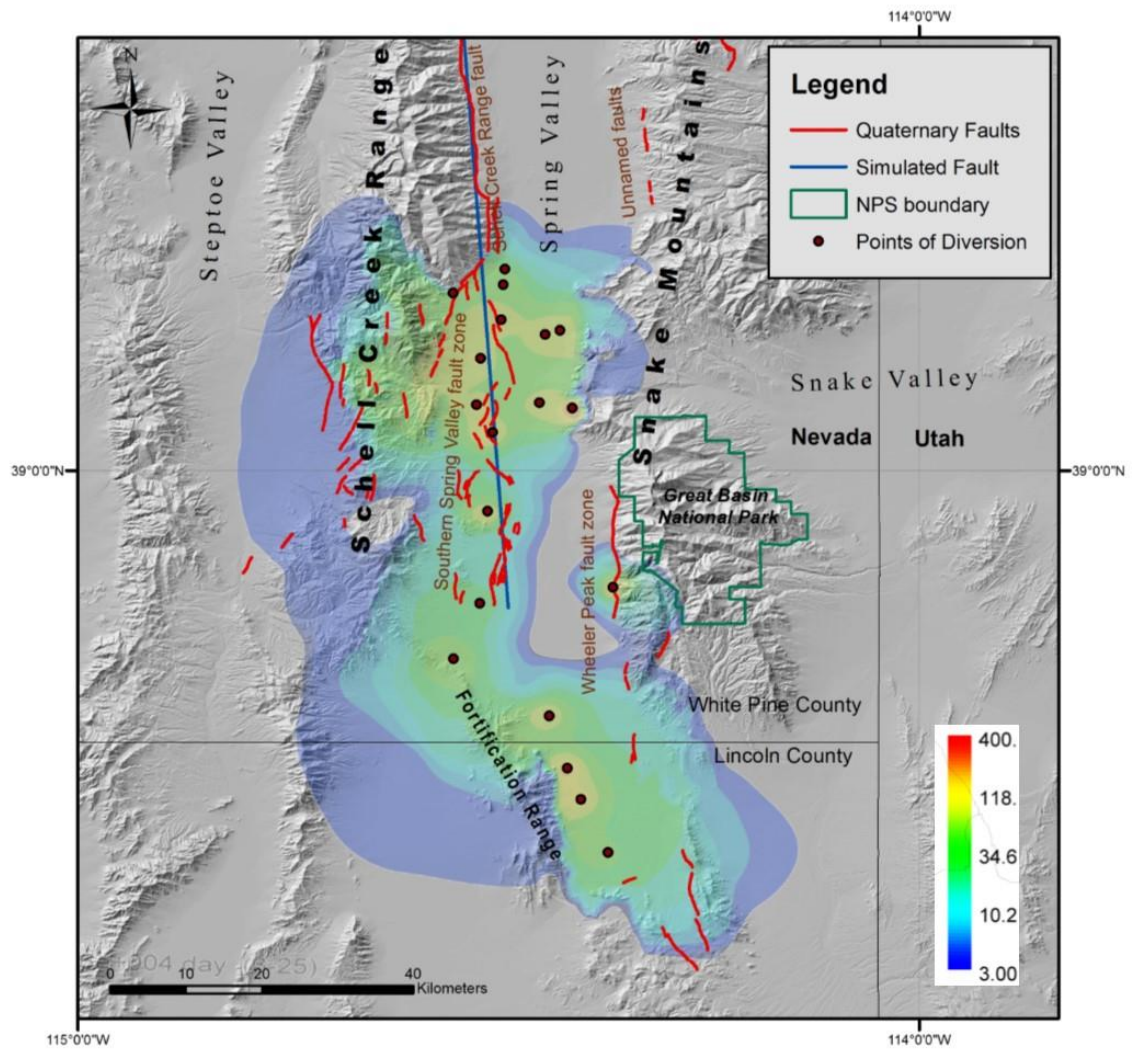


Figure 8. Drawdown (in feet) from pumping at a rate of $75.4 \times 10^6 \text{ m}^3/\text{year}$ (~61,127 acre-feet/year) for 50 years from Halford & Plume (2011) with points of diversion modified to locations in accordance with the Office of the Nevada State Engineer applications 54003 to 54021 in Spring Valley.

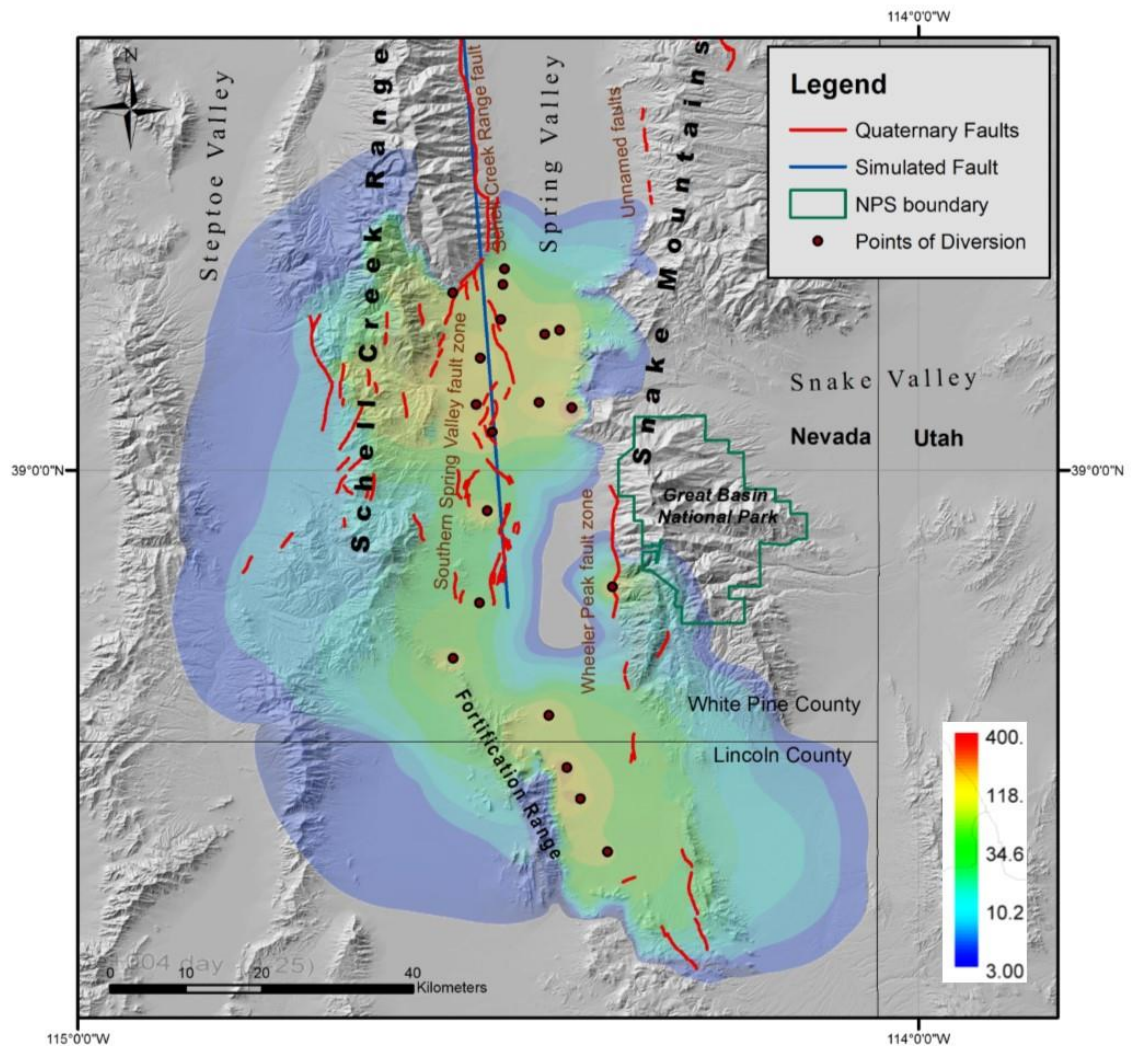


Figure 9. Drawdown (in feet) from pumping at a rate of $75.4 \times 10^6 \text{ m}^3/\text{year}$ ($\sim 61,127$ acre-feet/year) for **100** years from Halford & Plume (2011) with points of diversion modified to locations in accordance with the Office of the Nevada State Engineer applications 54003 to 54021 in Spring Valley.

Scenarios modeled

The approved pumping volume of $75.4 \times 10^6 \text{ m}^3/\text{year}$ for removal from Spring Valley provides a reference scenario for the current study. The modified Halford & Plume (2011)

groundwater model results provide output for pumping stress periods of 10, 50, and 100 years with pumping held constant at $75.4 \times 10^6 \text{ m}^3/\text{year}$ evenly divided between the 18 points of diversion. The model contains transient scenarios for up to 200 years, but this was assumed to be beyond the time scale for elastic response of the crust, and thus would not be sufficiently modeled under our methods. Subsurface stress is resolved on the Schell Creek Range fault and the Southern Spring Valley fault zone for unloading resulting from each stress period in the model.

Also, in consideration of local tectonics, two scenarios are modeled for resolution of stress on the Schell Creek Range fault and the Southern Spring Valley fault zone (outlined on **Figure 5**). In one scenario, purely normal motion is assumed from the east-west extensional tectonics assuming fault dip to be 60 degrees. In the second, strike-slip motion with a vertical fault assumption is modeled to account for the sense of shear transferred through the province from the plate boundary to the west (Hammond et al., 2014).

2D model description

We calculated ΔCFF using the 2D and 3D methods described above. First, two dimensional stress was simulated using equations 4-8 assuming a valley half width of $a=10 \text{ km}$. Force N (equations 4-6) was determined by taking a sum of N_i (equation 9) across all grid cells and dividing by the assumed load-length of the valley based on pumping well locations:

$$(18) \quad N = \frac{\sum_{i=1}^n N_i}{90,000 \text{ m}}.$$

A three-dimensional grid with cell sizes of 1 km^3 defined (X_0, Z_0) positions in the subsurface. The fault was located at the edge of the valley (load edge) with a dip of 60° to the east. The nodes in the (X_0, Z_0) grid corresponding to the fault location were identified, and then normal and shear

stress were calculated on these nodes using equations 7 & 8. Results were plotted to show ΔCFF vs. fault depth (**Figure 10**). A map view schematic of the 2D model load shape is included on **Figure 12**.

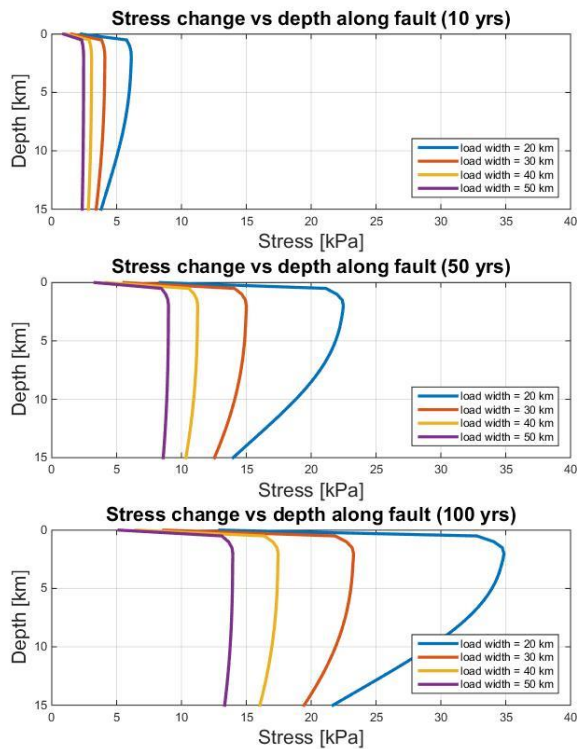


Figure 10. Vertical ΔCFF profile from the Schell Creek Range fault and southern Spring Valley fault zone. ΔCFF is plotted for various valley widths (2a in equations 4-6).

3D model description

Starting with an exported grid of drawdown values for each transient scenario (10 year, 50 year, & 100 year), N_i was calculated for each cell (equation 10). The stress tensors corresponding to locations of N_i were then resolved using equations 11 through 16. The strike of the fault is aligned approximately 2° west of north, or 358° azimuth, and the dip for a normal-

fault is assumed to be 60° . Using trigonometry combined with grid cell size and known fault geometry, the distance from the west edge of the model grid to the fault and the distance from the ground surface to the fault-trace in the subsurface could be identified. Two-dimensional linear interpolation of the stress tensor values was used to resolve the stress field at the location of the fault between grid nodes. To resolve the normal and shear stress acting on the fault, the coordinate system of the stress tensors was then transformed to be aligned with the strike and dip of the fault using equation 17 and the appropriate transformation matrix (L_z for the strike rotation, and L_y for the dip rotation). Based on the sense of slip, shear stress and normal stress in the fault plane corresponded to the τ_{xz} and τ_{xx} components, respectively. ΔCFF was then resolved using equation 3. A schematic diagram of the model setup is included as **Figure 11**, and the grid of the model area is included on **Figure 12**.

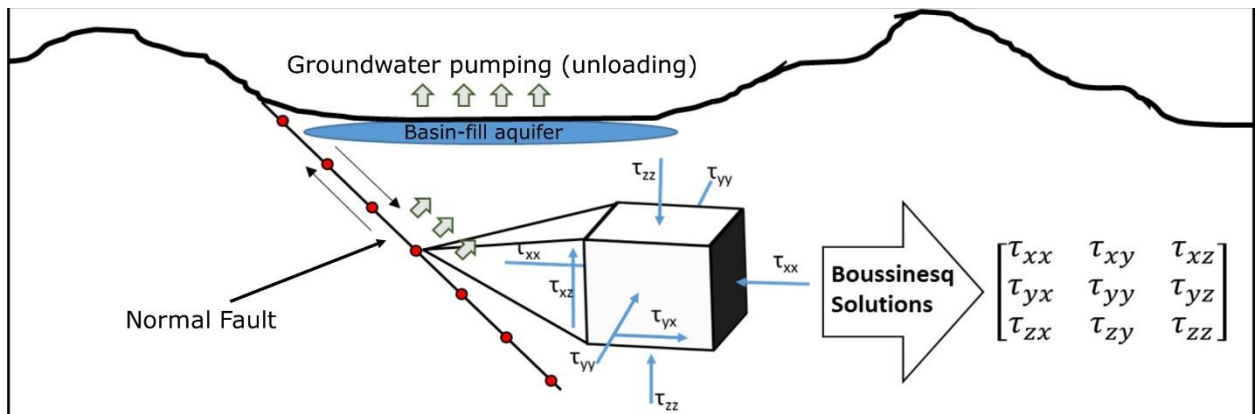


Figure 11. Schematic of model setup and methods

Contour plots of the ΔCFF on the fault plane from each transient scenario reflecting results from normal motion on the fault are shown on **Figure 13**, **Figure 14**, and **Figure 15**. Results plotted on **Figure 16** show a cross section of ΔCFF values at the beginning of the seismogenic zone, which is assumed to be 5 km depth.

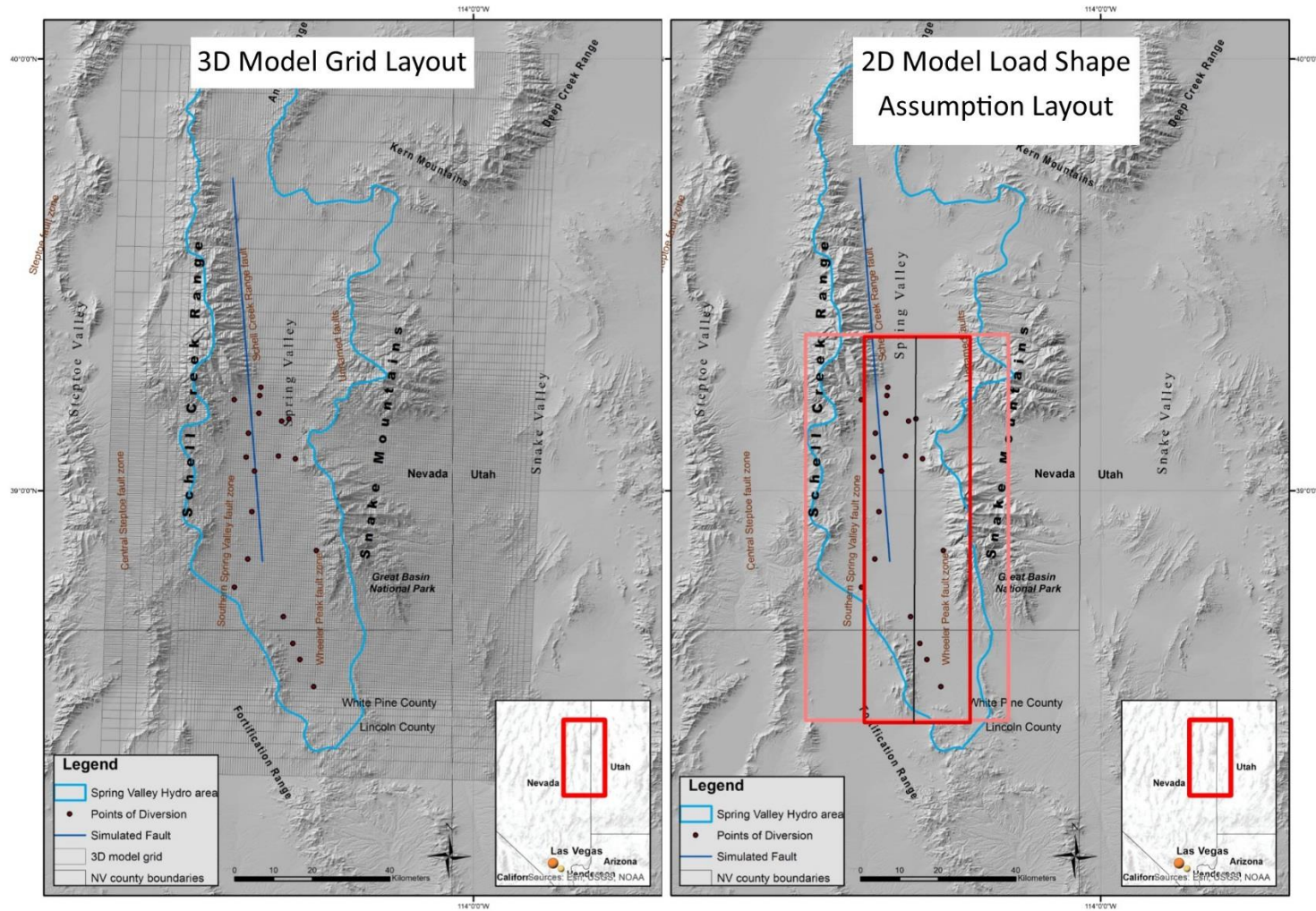


Figure 12. (Left) Layout of 3D model grid over Spring Valley (right) 2D rectangular load assumptions. The red outline is for 20 km load width assumption, and pink represents a 40 km load width assumption.

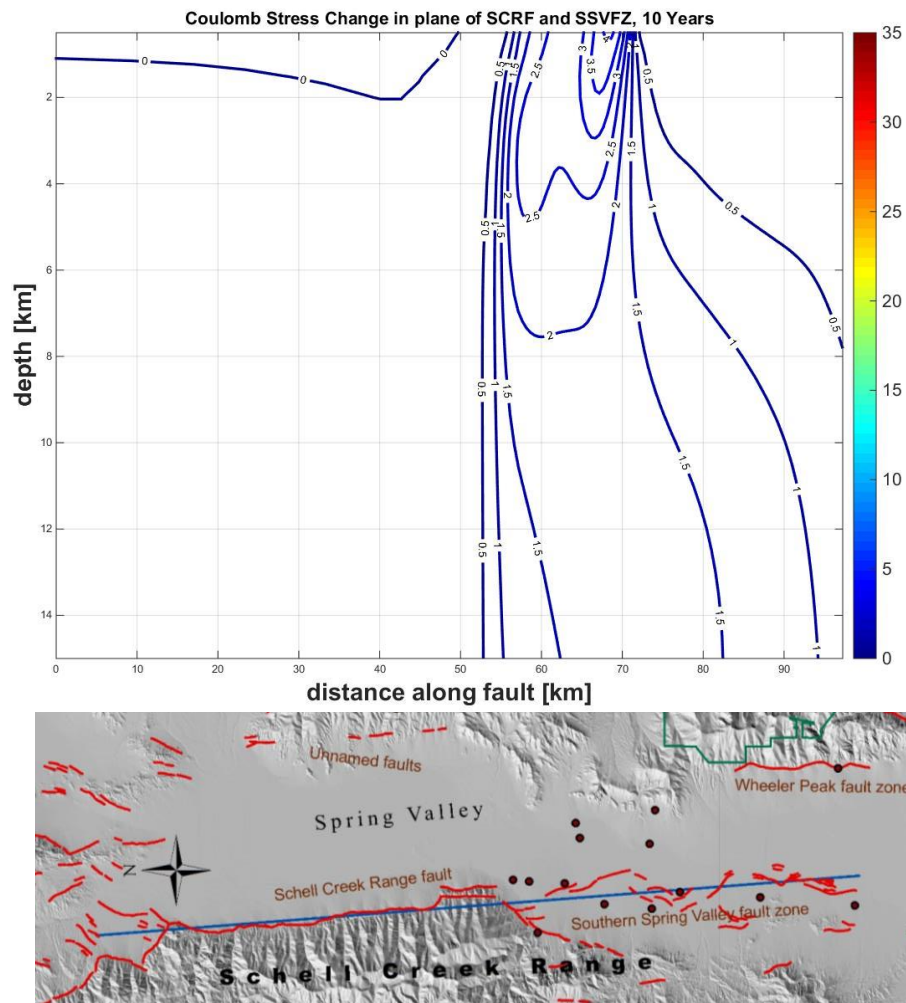


Figure 13. Δ CFE contoured in the fault plane of the SCRF and the SSVFC for 10 year scenario. Distance increases southward along x-axis.

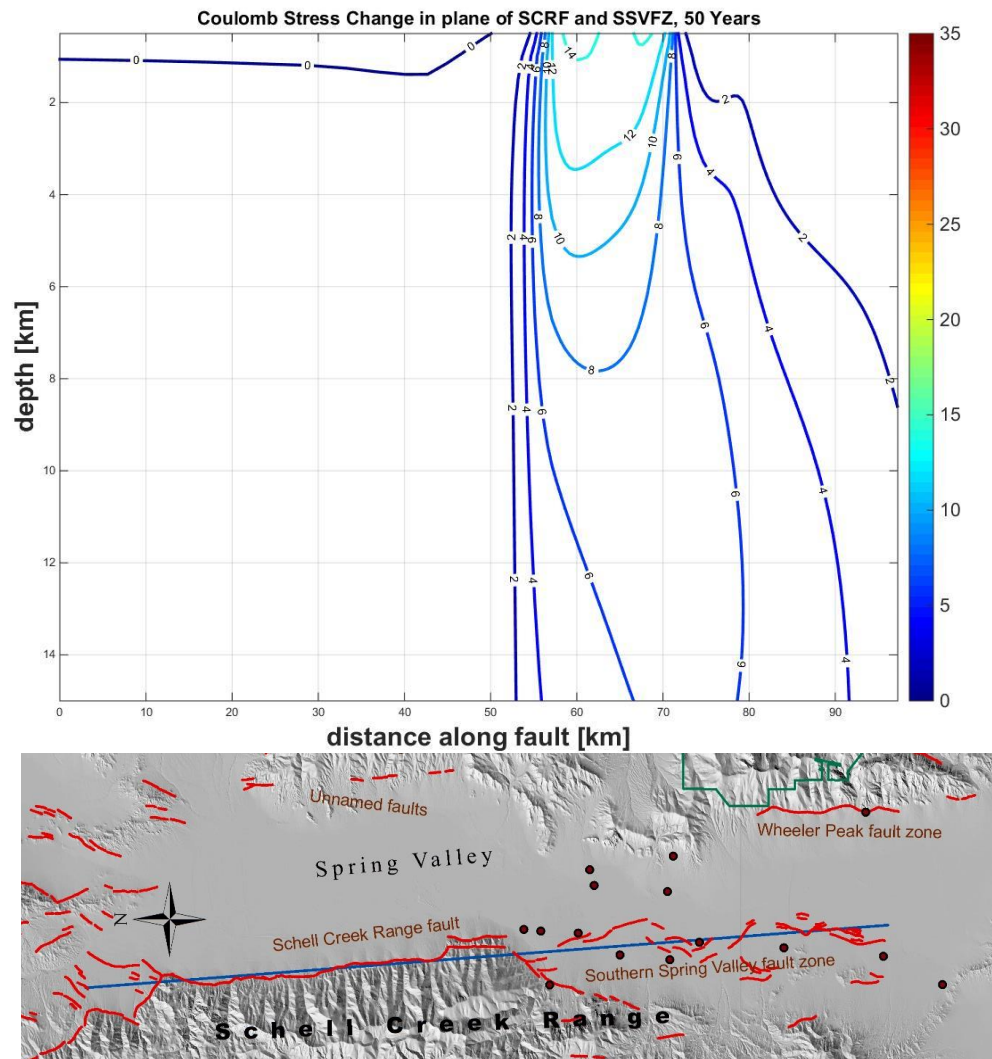


Figure 14. Δ CFF contoured in the fault plane of the SCRF and the SSVFZ for 50 year scenario. Distance increases southward along x-axis.

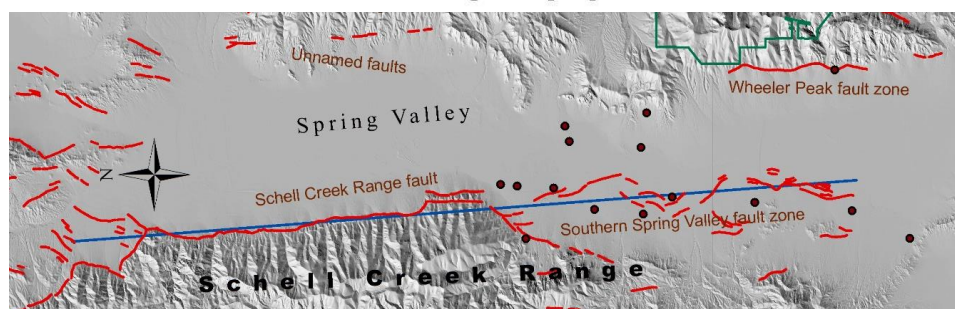
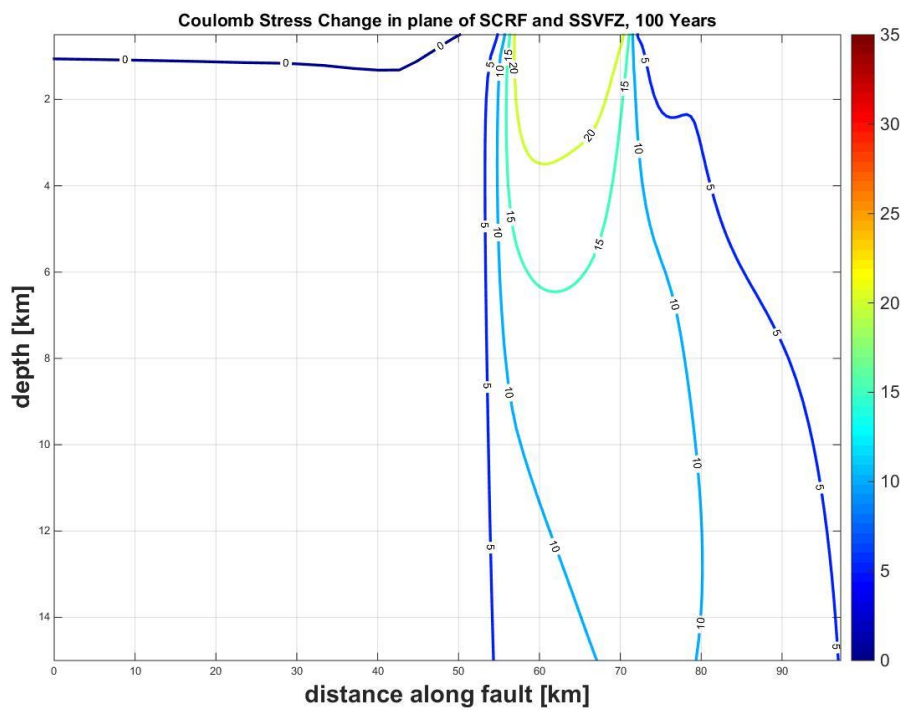


Figure 15. Δ CFF contoured in the fault plane of the SCRF and the SSVFC for 100 year scenario. Distance increases southward along x-axis.

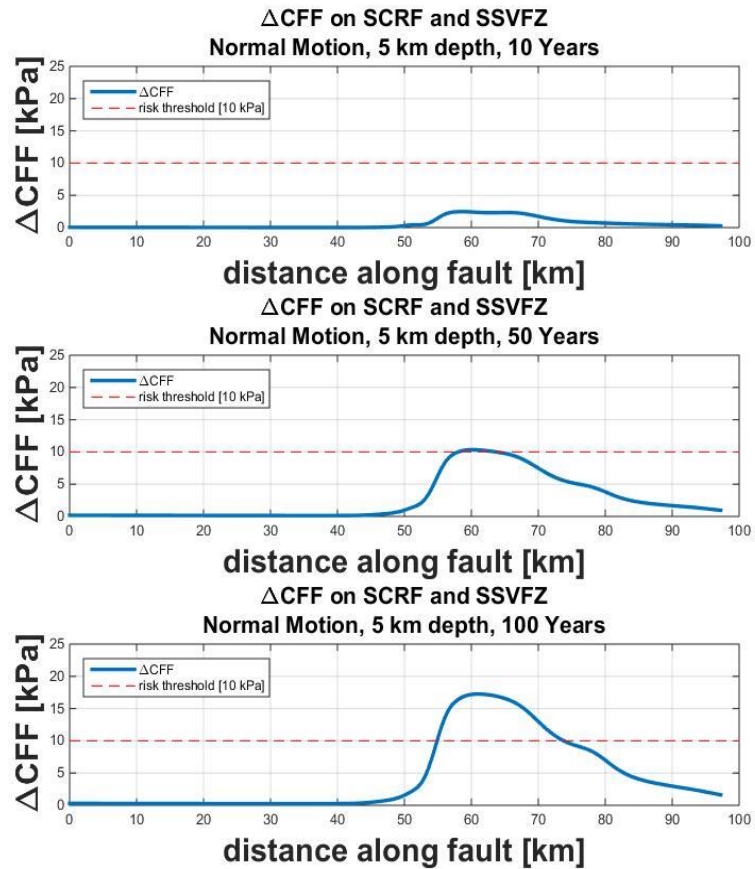


Figure 16. Δ CFF profile at 5 km depth along SCRF and SSVFZ. The dashed red line marks the 10 kPa value, which is used as a static stress triggering threshold. Values above this line represent greater risk of fault rupture.

For the strike slip scenario under the assumption of a vertical fault, transformation was not necessary for the stress tensor resolved (equations 11-16). The normal and shear components correspond to τ_{xx} and τ_{xy} , respectively. The Δ CFF was then resolved using equation 3.

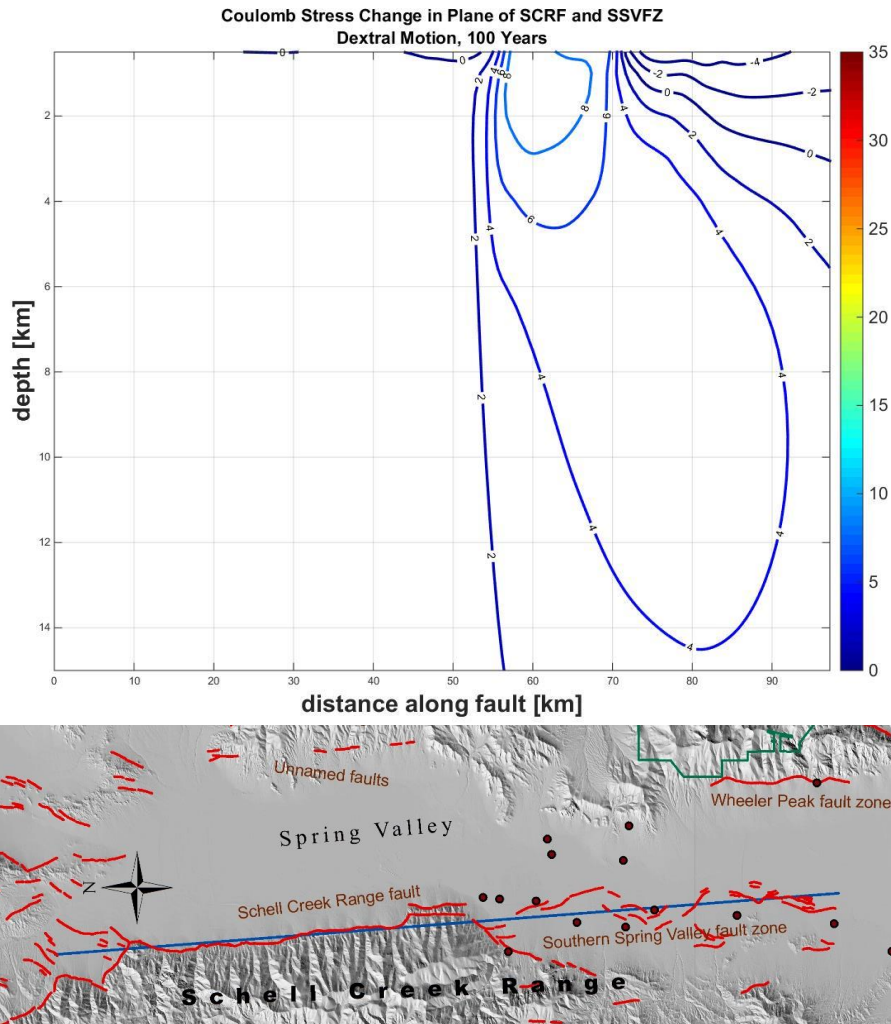


Figure 17. Δ CFF in plane of Schell Creek Range fault and Southern Spring Valley fault zone under the assumption of a vertical fault with purely dextral (right-lateral) motion for the **100** year pumping scenario. When compared with the normal-motion scenario, the Δ CFF here is much less. The Δ CFF did not reach above the 10 kPa threshold in either the 10 year, 50 year, or 100 year scenarios.

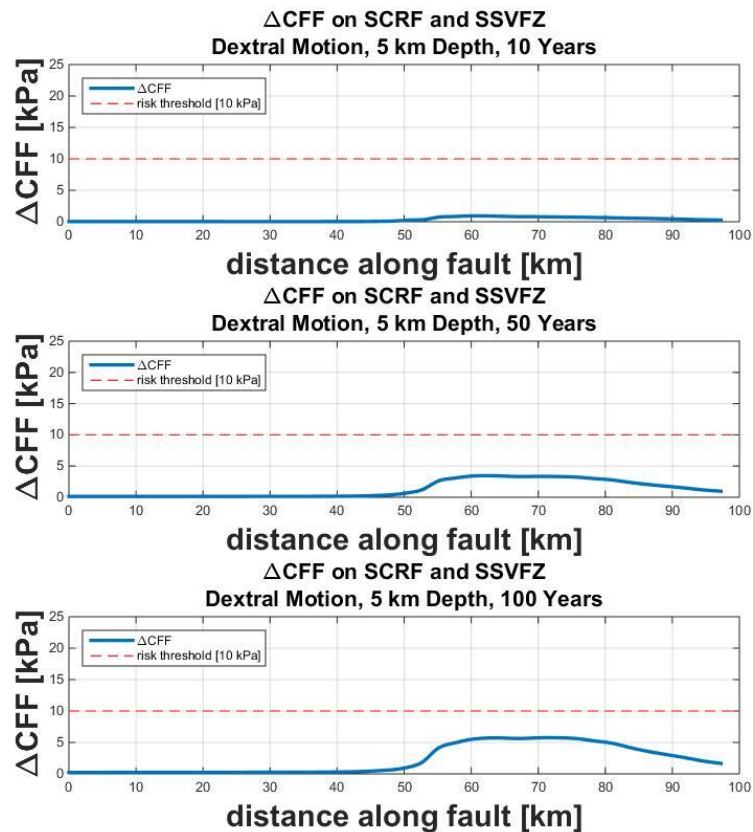


Figure 18. ΔCFF cross section at 5 km depth from the plane of the Schell Creek Range fault and Southern Spring Valley fault zone under the assumption of purely dextral (right-lateral) motion for the 10, 50, and 100 year pumping scenario. No transient pumping scenarios showed enough ΔCFF increase to surpass the 10 kPa threshold.

Discussion

Comparison of 2D vs. 3D stress modeling results

2D modeling shows an inverse relationship of the modeled parameter for load-width to ΔCFF ; as load width increases, ΔCFF decreases (**Figure 10**) (**Equations 4-6**). Sensitivity of this parameter in analysis is high and must be correctly determined for accurate subsurface stress results. For example, it was initially assumed that groundwater withdrawal would be contained within the reaches of the basin fill, which meant the modeled load-width was assumed

equivalent to largest valley width in the area of groundwater pumping (20 km wide, $a = 10$ km) (**Figure 12**). The ΔCFF magnitudes resolved with this load-width for pumping scenarios of 50 years or longer were approximately twice those modeled by the 3D modeling method (**Figure 10 & Figure 16**).

The groundwater flow model used in this work shows that load-width increases with increasing pumping duration (**Figure 9**). Basin boundaries may not provide an effective constraint on load-width when pumping over longer timescales. Comparison supports this: at 10 years' time, when the groundwater flow model shows drawdown area to be the smallest, ΔCFF from 2D modeling results using a valley width of 20 km are very similar to the 3D modeling results, both around 6 kPa at a depth of 5 km. At 100 years' time, 2D results best match the 3D model under the 40 km load-width scenario (at 5 km depth: 2D results = ~ 17 kPa vs. 3D results = ~ 17 kPa). The approximate valley widths that match 2D modeling results to 3D results are supported by the 3D groundwater flow model results (**Figure 7, Figure 8, & Figure 9**)(Halford & Plume, 2011) despite the large east-west variation of load thickness (**Figure 7, Figure 8, & Figure 9**). Because of this, estimation of an appropriate load-width while using 2D modeling methods under predictive scenarios may be difficult without a 3D groundwater flow model.

Comparison of normal and strike slip motion

The dextral motion scenario resulted in lower values of ΔCFF on the fault (**Figure 17 & Figure 18**). Because modeling shows a larger ΔCFF increase on an angled fault (**Figure 16**), a vertical fault would experience less unclamping from unloading from above when compared with a fault dipping at any angle. At 5 km depth, all scenarios showed stress changes less than the threshold value (**Figure 18**). Constraints on actual fault motion are weak due to the lack of

modern seismic activity, although ΔCFF from dextral slip on a vertical fault can be classified to have little effect on increasing potential for seismic fault-rupture in the area.

Comparison of Coulomb stress change in Spring Valley case study with previous study results

Initially, comparison of surface stress change from load removal in large-scale geologic situations with modern anthropogenic surface stress changes (**Figure 2**) opened a question of whether similarities in surface stress would translate to similar effects to fault slip rates and seismicity. This correlation was too simple to draw conclusions from, although the relationship prompted development of the methods described in previous sections to categorize large-scale hydrospheric mass changes as increasing seismic potential or not. The method developed can be used for general analysis of both past and future scenarios involving large-scale mass changes. Application of this method to potential pumping scenarios in Spring Valley, Nevada has shown that long term pumping at proposed pumping rates will induce a ΔCFF on the fault that brings it above the risk-of-failure threshold, which may in-turn increase potential for triggering seismicity and/or increase rate of seismicity occurrence on the fault. In **Figure 19**, ranges of ΔCFF computed for pumping scenarios in Spring Valley are plotted beside computed values of ΔCFF for similar scenarios of increased seismicity or induced earthquakes resulting from observed hydrospheric mass changes.

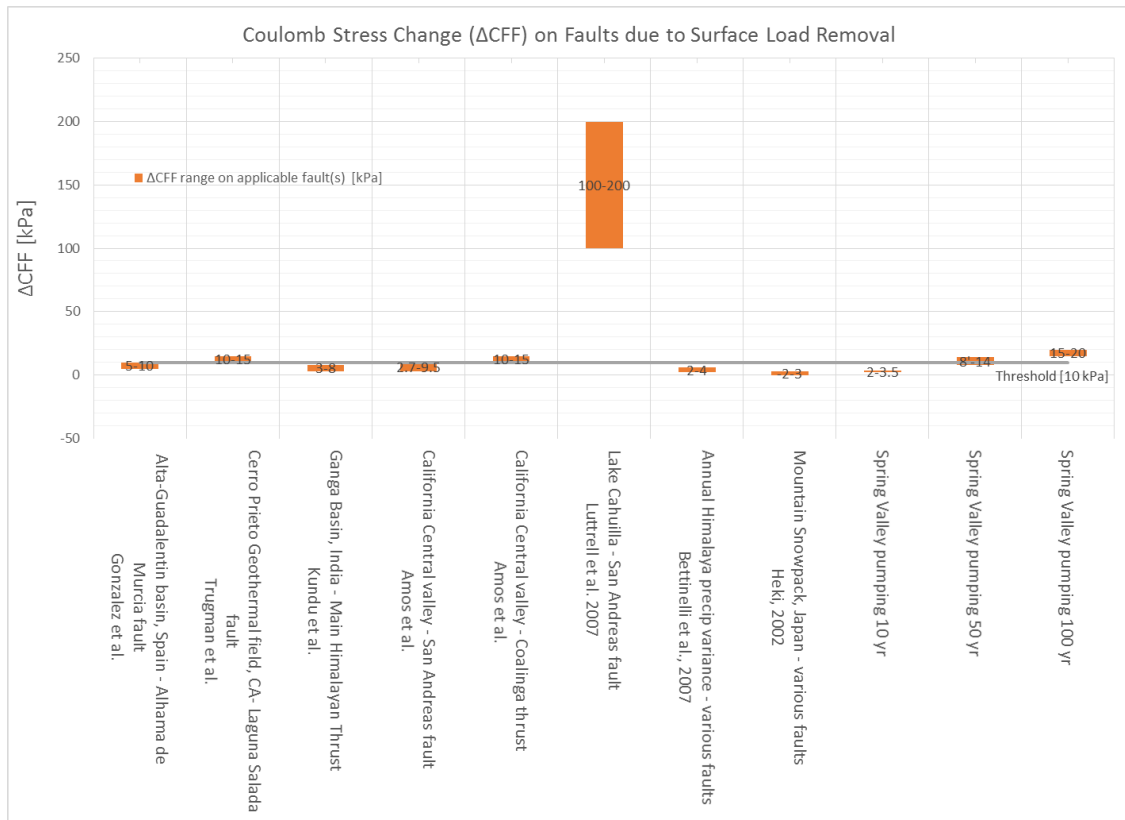


Figure 19. Comparison of ΔCFF ranges for hydrologic mass unloading with the Spring Valley pumping scenarios (10 year, 50 year, and 100 year).

Comparison of ΔCFF values for these instances presents a framework to both support the threshold value of 10 kPa and also to provide reference for results found in the case of seismic fault-rupture potential increase from pumping in Spring Valley.

Method applications

Groundwater aquifers throughout the world are entering a stressed classification resulting from overuse (Richey et al., 2015). Coincident with heavily used aquifers is the potential for increasing potential for fault-rupture in pumping areas. The method developed in this work can easily be applied to locations where unloading from groundwater pumping is known or can be estimated. Paired with information such as fault location, geometry, and sense

of slip, analysis for an increase of fault-rupture potential can inform if mitigation measures are necessary. In the case of Spring Valley where pumping results in an increase of fault-rupture potential, a simple decrease in pumping volume would likely result in lowering this potential. But with increasing demand, lowering pumping volume may not be plausible, thus the 3D model allows for design of appropriate alteration of pumping patterns or volumes in stressed areas to decrease the stress on critical areas of the fault.

Considerations under the given method

A general source of uncertainty in any prediction related to fault-rupture triggering is the prevailing state of stress on the fault in question. Faults are generally locked at a state of stress close to the strength of the fault, even in stable intraplate areas (Grasso & Sornette, 1998; Townend & Zoback, 2000; Zoback & Harjes, 1997). Because of this, the fault is sensitive to changes in the balance expressed in equation 2, although the degree of sensitivity to perturbations in shear or normal stress cannot now be quantified. The threshold used in this work is based on a probabilistic model; it does not mark a mechanical failure threshold and is used only as a reference for an increased potential for triggering seismic rupture along the fault. In the case of Spring Valley, existing seismic hazard is low, thus it is likely that stress in excess of the threshold will not equate to imminent rupture.

Addressing the increase or decrease of either seismic risk or seismic hazard is beyond the scope of this study, and thus reference is made to the increasing or decreasing degree of potential of a fault plane toward failure that results in a seismic event. Methods presented are not predictive of seismic event timing or magnitude, as the onset of a rupture is not diagnostic of final rupture size (Meier, Heaton, & Clinton, 2016).

Also, other groundwater flow models developed for the Spring Valley area (Burns & Drici, 2011; Myers, 2011) predict different degrees of drawdown from pumping. Just as stress on the fault plane is sensitive to load area in the 2D modeling scenarios, it would follow that 3D stress analysis would have sensitivity to groundwater model results used for input to stress modeling. For this study, a publicly available groundwater model was chosen that was peer-reviewed and developed by experienced groundwater modelers (Halford & Plume, 2011). Bias in modeling may present concern in some situations, but treatment of this issue is not considered in this study.

Conclusions

In the Spring Valley case study, an increase of potential for seismic rupture was discovered along the Schell Creek Range fault and/or the Southern Spring Valley fault zone for pumping scenarios lasting longer than 50 years under a normal-faulting regime, while likelihood of fault-rupture also increases with pumping duration (**Figure 13, Figure 14, Figure 15, & Figure 16**). Δ CFF resolved on the Fault for the 10 year scenario is below the threshold, although pumping-induced Δ CFF as low as 5 kPa has still been implicated in triggering earthquakes (**Table 1**).

The 50 year and 100 year predictive pumping scenarios showed a Coulomb stress change on a significant portion of the Schell Creek Range fault and Southern Spring Valley fault zone above the static stress triggering threshold of 10 kPa. Potential for rupture on the Schell Creek Range fault and Southern Spring Valley fault zone would be increased by groundwater pumping at the proposed amount of $75.4 \times 10^6 \text{ m}^3$ annually when pumping would approach or exceed 50 years. In the case of a vertical strike-slip fault in the valley exhibiting dextral motion,

results show that this scenario would not significantly contribute to seismic rupture potential increase, as ΔCFF values are below the 10 kPa threshold in the seismogenic zone.

The method presented can be used for similar scenarios to determine increase of potential for triggering fault-rupture resulting from groundwater pumping, although determinations are approximate and subject to error based on prevailing state of stress on the fault with respect to the critical value. Greater magnitude between the prevailing state of stress on the fault and the critical value for failure means lower potential for triggering fault-rupture. Also, 2D analytical solutions in modeling subsurface stress changes are sensitive to modeled load area, demonstrating the value of groundwater flow models for estimation of load removal area.

References

- Amos, C. B., Audet, P., Hammond, W. C., Buergermann, R., Johanson, I. A., & Blewitt, G. (2014). Uplift and seismicity driven by groundwater depletion in central California. *Nature*, 509(7501), 483-+. doi:10.1038/nature13275
- Anderson, G., & Johnson, H. (1999). A new statistical test for static stress triggering: Application to the 1987 Superstition Hills earthquake sequence. *Journal of Geophysical Research-Solid Earth*, 104(B9), 20153-20168. doi:10.1029/1999jb900200
- Bartley, J. M., & Wernicke, B. P. (1984). THE SNAKE RANGE DECOLLEMENT INTERPRETED AS A MAJOR EXTENSIONAL SHEAR ZONE. *Tectonics*, 3(6), 647-657. doi:10.1029/TC003i006p00647
- Bennett, R. A., Wernicke, B. P., & Davis, J. L. (1998). Continuous GPS measurements of contemporary deformation across the northern Basin and Range province. *Geophysical Research Letters*, 25(4), 563-566. doi:10.1029/98gl00128
- Bennett, R. A., Wernicke, B. P., Niemi, N. A., Friedrich, A. M., & Davis, J. L. (2003). Contemporary strain rates in the northern Basin and Range province from GPS data. *Tectonics*, 22(2). doi:10.1029/2001tc001355
- Bettinelli, P., Avouac, J. P., Flouzat, M., Bollinger, L., Ramillien, G., Rajaure, S., & Sapkota, S. (2008). Seasonal variations of seismicity and geodetic strain in the Himalaya induced by surface hydrology. *Earth and Planetary Science Letters*, 266(3-4), 332-344. doi:10.1016/j.epsl.2007.11.021
- Boussinesq, J. (1885). *Application des potentiels à l'étude de l'équilibre et du mouvement des solides élastiques: principalement au calcul des déformations et des pressions que produisent, dans ces solides, des efforts quelconques exercés sur une petite partie de leur surface ou de leur intérieur: mémoire suivi de notes étendues sur divers points de physique, mathématique et d'analyse* (Vol. 4): Gauthier-Villars.
- Burns, A. G., & Drici, W. (2011). *Hydrology and water resources of Spring, Cave, Dry Lake, and Delamar valleys, Nevada and vicinity*. Retrieved from Presentation to the Office of the Nevada State Engineer:
- Christiansen, L. B., Hurwitz, S., & Ingebritsen, S. E. (2007). Annual modulation of seismicity along the San Andreas Fault near Parkfield, CA. *Geophysical Research Letters*, 34(4). doi:10.1029/2006gl028634
- Depolo, C. M., & Anderson, J. G. (2000). Estimating the slip rates of normal faults in the Great Basin, USA. *Basin Research*, 12(3-4), 227-240. doi:10.1046/j.1365-2117.2000.00131.x
- Dohrenwend, J. C., Schell, B. A., & Moring, B. C. (1991). *Reconnaissance photogeologic map of young faults in the Ely 1 degree by 2 degrees Quadrangle, Nevada and Utah* (2181). Retrieved from <http://pubs.er.usgs.gov/publication/mf2181>
- Ellsworth, W. L. (2013). Injection-Induced Earthquakes. *Science*, 341(6142), 142-+. doi:10.1126/science.1225942

- Farrell, W. E. (1972). DEFORMATION OF EARTH BY SURFACE LOADS. *Reviews of Geophysics and Space Physics*, 10(3), 761-&. doi:10.1029/RG010i003p00761
- Gonzalez, P. J., Tiampo, K. F., Palano, M., Cannavo, F., & Fernandez, J. (2012). The 2011 Lorca earthquake slip distribution controlled by groundwater crustal unloading. *Nature Geoscience*, 5(11), 821-825. doi:10.1038/ngeo1610
- Gourmelen, N., & Amelung, F. (2005). Postseismic mantle relaxation in the Central Nevada Seismic Belt. *Science*, 310(5753), 1473-1476. doi:10.1126/science.1119798
- Grasso, J. R., & Sornette, D. (1998). Testing self-organized criticality by induced seismicity. *Journal of Geophysical Research-Solid Earth*, 103(B12), 29965-29987. doi:10.1029/97jb01344
- Halford, K. J., & Plume, R. W. (2011). *Potential effects of groundwater pumping on water levels, phreatophytes, and spring discharges in Spring and Snake Valleys, White Pine County, Nevada, and adjacent areas in Nevada and Utah*. Retrieved from
- Hammond, W. C., Blewitt, G., & Kreemer, C. (2014). Steady contemporary deformation of the central Basin and Range Province, western United States. *Journal of Geophysical Research-Solid Earth*, 119(6), 5235-5253. doi:10.1002/2014jb011145
- Hammond, W. C., & Thatcher, W. (2004). Contemporary tectonic deformation of the Basin and Range province, western United States: 10 years of observation with the Global Positioning System. *Journal of Geophysical Research-Solid Earth*, 109(B8). doi:10.1029/2003jb002746
- Hampel, A., & Hetzel, R. (2006). Response of normal faults to glacial-interglacial fluctuations of ice and water masses on Earth's surface. *Journal of Geophysical Research-Solid Earth*, 111(B6). doi:10.1029/2005jb004124
- Hampel, A., Hetzel, R., & Densmore, A. L. (2007). Postglacial slip-rate increase on the Teton normal fault, northern Basin and Range Province, caused by melting of the Yellowstone ice cap and deglaciation of the Teton Range? *Geology*, 35(12), 1107-1110. doi:10.1130/g24093a.1
- Hampel, A., Hetzel, R., & Maniatis, G. (2010). Response of faults to climate-driven changes in ice and water volumes on Earth's surface. *Philosophical Transactions of the Royal Society a-Mathematical Physical and Engineering Sciences*, 368(1919), 2501-2517. doi:10.1098/rsta.2010.0031
- Hampel, A., Hetzel, R., Maniatis, G., & Karow, T. (2009). Three-dimensional numerical modeling of slip rate variations on normal and thrust fault arrays during ice cap growth and melting. *Journal of Geophysical Research-Solid Earth*, 114. doi:10.1029/2008jb006113
- Harbaugh, A. W., Banta, E. R., Hill, M. C., & McDonald, M. G. (2000). *MODFLOW-2000, The U.S. Geological Survey Modular Ground-Water Model - User Guide to Modularization Concepts and the Ground-Water Flow Process (2000-92)*. Retrieved from <http://pubs.er.usgs.gov/publication/ofr200092>

- Hardebeck, J. L., Nazareth, J. J., & Hauksson, E. (1998). The static stress change triggering model: Constraints from two southern California aftershock sequences. *Journal of Geophysical Research-Solid Earth*, 103(B10), 24427-24437. doi:10.1029/98jb00573
- Heki, K. (2003). Snow load and seasonal variation of earthquake occurrence in Japan. *Earth and Planetary Science Letters*, 207(1-4), 159-164. doi:10.1016/s0012-821x(02)01148-2
- Hetzl, R., & Hampel, A. (2005). Slip rate variations on normal faults during glacial-interglacial changes in surface loads. *Nature*, 435(7038), 81-84. doi:10.1038/nature03562
- Jackson, J. A. (1987). Active normal faulting and crustal extension. *Geological Society, London, Special Publications*, 28(1), 3-17. doi:10.1144/gsl.sp.1987.028.01.02
- Jaeger, J. C., Cook, N. G. W., & Zimmerman, R. (2007). *Fundamentals of Rock Mechanics, 4th edition* (Fourth Edition ed.): Wiley-Blackwell
- Karow, T., & Hampel, A. (2010). Slip rate variations on faults in the Basin-and-Range Province caused by regression of Late Pleistocene Lake Bonneville and Lake Lahontan. *International Journal of Earth Sciences*, 99(8), 1941-1953. doi:10.1007/s00531-009-0496-3
- King, G. C. P., Stein, R. S., & Lin, J. (1994). STATIC STRESS CHANGES AND THE TRIGGERING OF EARTHQUAKES. *Bulletin of the Seismological Society of America*, 84(3), 935-953.
- Koehler, R. D., & Wesnousky, S. G. (2011). Late Pleistocene regional extension rate derived from earthquake geology of late Quaternary faults across the Great Basin, Nevada, between 38.5 degrees N and 40 degrees N latitude. *Geological Society of America Bulletin*, 123(3-4), 631-650. doi:10.1130/b30111.1
- Kundu, B., Vissa, N. K., & Gahalaut, V. K. (2015). Influence of anthropogenic groundwater unloading in Indo-Gangetic plains on the 25 April 2015 Mw 7.8 Gorkha, Nepal earthquake. *Geophysical Research Letters*, 42(24). doi:10.1002/2015gl066616
- Lockner, D. A., & Beeler, N. M. (1999). Premonitory slip and tidal triggering of earthquakes. *Journal of Geophysical Research-Solid Earth*, 104(B9), 20133-20151. doi:10.1029/1999jb900205
- Love, A. E. H. (1929). The stress produced in a semi-infinite solid by pressure on part of the boundary. *Philosophical Transactions of the Royal Society of London. Series A, Containing Papers of a Mathematical or Physical Character*, 228, 377-420.
- Luttrell, K., Sandwell, D., Smith-Konter, B., Bills, B., & Bock, Y. (2007). Modulation of the earthquake cycle at the southern San Andreas fault by lake loading. *Journal of Geophysical Research-Solid Earth*, 112(B8). doi:10.1029/2006jb004752
- McGarr, A., Simpson, D., & Seeber, L. (2002). Case histories of induced and triggered seismicity *International Handbook of Earthquake and Engineering Seismology* (1st ed., Vol. 8). Waltham, MA: Academic Press.
- Meier, M.-A., Heaton, T., & Clinton, J. (2016). Evidence for Universal Earthquake Rupture Initiation Behavior. *Geophysical Research Letters*, n/a-n/a. doi:10.1002/2016GL070081

- Miller, E. L., Dumitru, T. A., Brown, R. W., & Gans, P. B. (1999). Rapid Miocene slip on the Snake Range-Deep Creek Range fault system, east-central Nevada. *Geological Society of America Bulletin*, 111(6), 886-905. doi:10.1130/0016-7606(1999)111<0886:rmsots>2.3.co;2
- Myers, T. (2011). *Hydrogeology of Spring Valley and surrounding areas, Part B: Groundwater model of Snake and Spring valleys, and surrounding areas*. Retrieved from Presented to the Office of the Nevada State Engineer:
- Prudic, D. E., Harrill, J. R., & Burbey, T. J. (1995). *Conceptual evaluation of regional ground-water flow in the carbonate-rock province of the Great Basin, Nevada, Utah and adjacent states*. Retrieved from
- Reasenber, P. A., & Simpson, R. W. (1992). RESPONSE OF REGIONAL SEISMICITY TO THE STATIC STRESS CHANGE PRODUCED BY THE LOMA-PRIETA EARTHQUAKE. *Science*, 255(5052), 1687-1690. doi:10.1126/science.255.5052.1687
- Richey, A. S., Thomas, B. F., Lo, M.-H., Reager, J. T., Famiglietti, J. S., Voss, K., . . . Rodell, M. (2015). Quantifying renewable groundwater stress with GRACE. *Water Resources Research*, 51(7), 5217-5238. doi:10.1002/2015wr017349
- Southern Nevada Water Authority. (2012). *Clark, Lincoln, and White Pine Counties Groundwater Development project: Conceptual Plan of Development*. Retrieved from Las Vegas, Nevada: http://www.snwa.com/assets/pdf/ws_gdp_copd.pdf
- Stein, R. S. (1999). The role of stress transfer in earthquake occurrence. *Nature*, 402(6762), 605-609. doi:10.1038/45144
- Toda, S., Stein, R. S., & Sagiya, T. (2002). Evidence from the AD 2000 Izu islands earthquake swarm that stressing rate governs seismicity. *Nature*, 419(6902), 58-61. doi:10.1038/nature00997
- Townend, J., & Zoback, M. D. (2000). How faulting keeps the crust strong. *Geology*, 28(5), 399-402. doi:10.1130/0091-7613(2000)28<399:hfkctcs>2.0.co;2
- Trugman, D. T., Borsa, A. A., & Sandwell, D. T. (2014). Did stresses from the Cerro Prieto Geothermal Field influence the El Mayor-Cucapah rupture sequence? *Geophysical Research Letters*, 41(24), 8767-8774. doi:10.1002/2014gl061959
- Turcotte, D. L., & Schubert, G. (2002). *Geodynamics* (2nd ed.). New York, NY: Cambridge University Press.
- Turpeinen, H., Hampel, A., Karow, T., & Maniatis, G. (2008). Effect of ice sheet growth and melting on the slip evolution of thrust faults. *Earth and Planetary Science Letters*, 269(1-2), 230-241. doi:10.1016/j.epsl.2008.02.017
- Twiss, R. J., & Moores, E. M. (1992). *Structural Geology*. New York: W.H. Freeman and Company.
- United States Geological Survey, & Nevada Bureau of Mines and Geology (Producer). (2016, June 3, 2016). Quaternary fault and fold database for the United States. Retrieved from <http://earthquake.usgs.gov/hazards/qfaults/>

- Welch, A. H., Bright, D. J., & Knochenmus, L. A. (2008). *Water Resources of the Basin and Range Carbonate-Rock Aquifer System, White Pine County, Nevada, and Adjacent Areas in Nevada and Utah* (2007-5261). Retrieved from <http://pubs.er.usgs.gov/publication/sir20075261>
- Zoback, M. D., & Harjes, H. P. (1997). Injection-induced earthquakes and crustal stress at 9 km depth at the KTB deep drilling site, Germany. *Journal of Geophysical Research-Solid Earth*, 102(B8), 18477-18491. doi:10.1029/96jb02814